

DEVELOPMENT OF A COMMERCIAL MICRO-SPECTROMETER FOR REMOTE
FIELD DEPLOYMENT

by

Rantaj Singh

Copyright © Rantaj Singh 2022

A Thesis Submitted to the Faculty of the

WYANT COLLEGE OF OPTICAL SCIENCES

In Partial Fulfillment of the Requirements

For the Degree of

MASTER OF SCIENCE

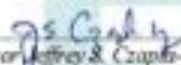
In the Graduate College

THE UNIVERSITY OF ARIZONA

2022

THE UNIVERSITY OF ARIZONA
GRADUATE COLLEGE

As members of the Master's Committee, we certify that we have read the thesis prepared by **Rantaj Singh**, titled *Development of a Commercial Micro-spectrometer for Remote Field Deployment* and recommend that it be accepted as fulfilling the dissertation requirement for the Master's Degree.



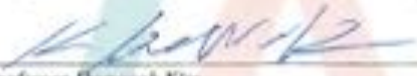
Professor Jeffrey S. Czupka-Myers

Date: 12 APR 2022



Professor R. John Kishel

Date: 4/12/2022



Professor Daewook Kim

Date: 4/12/2022

Final approval and acceptance of this thesis is contingent upon the candidate's submission of the final copies of the thesis to the Graduate College.

I hereby certify that I have read this thesis prepared under my direction and recommend that it be accepted as fulfilling the Master's requirement.



Professor Jeffrey S. Czupka-Myers
Master's Thesis Committee Chair
Wyant College of Optical Sciences

Date: 12 APR 2022



Acknowledgements

I would first and foremost like to thank my advisor, Dr. Jeffrey Czapla-Myers, for his guidance and support in my research work and academics throughout my undergraduate and graduate career.

I also would like to thank my committee, Dr. John Koshel and Dr. Daewook Kim, for their time and commitment to the work of this thesis.

I would like to thank Nik Anderson for his mentorship. Without Nik's mentorship I would not be the engineer or person that I am today. I am truly grateful for his guidance, and I would also like to thank him for his contributions to the work in this thesis.

I am also extremely grateful to the Remote Sensing Group at the University of Arizona for allowing me to grow as both a student and a researcher. I would like to thank Charles Burkhart, Rob Kingston, and Dr. Stu Biggar for their contributions to this thesis and my personal growth.

Table of Contents

LIST OF FIGURES	6
LIST OF TABLES	8
ABSTRACT	9
CHAPTER 1: INTRODUCTION	10
1.1 Overview of Thesis	10
1.2 Remote Sensing Group	11
1.2.1 Background	11
1.2.2 Ground-Based Vicarious Radiometric Calibration	12
1.2.3 Radiometric Calibration Test Site	15
1.3 Spectrometer Mega Arduino	18
CHAPTER 2: DEVICE DESCRIPTION	22
2.1 Requirements.....	22
2.2 Description of Device	24
CHAPTER 3: PROTOTYPING	27
3.1 Hamamatsu Evaluation Circuit.....	27
3.1.1 Components	27
3.1.2 Evaluation Software.....	28
3.2 Housing	32
3.2.1 Reasons for Housing	32
3.2.2 Design Process	33
3.2.3 Final Design.....	36
CHAPTER 4: CHARACTERIZATION	41
4.1 Testing	41
4.1.1 Linearity	41
4.1.2 Field of View	43
4.1.3 Optimal Integration Time for Field Use.....	44
4.1.4 Signal to Noise Ratio	45
4.1.5 Dark Noise Characterization.....	46
4.1.6 Temperature Effects	47
4.1.7 Stray Light	48
4.1.8 Spectral Characterization	49
4.1.9 Repeatability.....	50
4.1.10 Surface Reflectance Retrieval	50
4.2 Radiometric Calibration.....	52
CHAPTER 5: RESULTS	54
5.1 Characterization Results	54
5.1.1 Linearity	54
5.1.2 Field of View	57
5.1.3 Optimal Integration Time for Field Use.....	58
5.1.4 Signal to Noise Ratio	59
5.1.5 Dark Noise Characterization.....	60
5.1.6 Temperature Effects	60
5.1.7 Stray Light	62
5.1.8 Spectral Characterization	62
5.1.9 Repeatability.....	64
5.1.10 Surface Reflectance Retrieval	64
5.2 Radiometric Calibration Results.....	65
CHAPTER 6: DISCUSSION AND FUTURE WORK	67
6.1 Discussion of Laboratory Characterization	67

6.2 Summary of Thesis	70
6.3 Future Work	71
APPENDIX A: HOUSING DRAWINGS	73
A.1 Front View of Housing	74
A.2 Side View of Housing	75
A.3 Top View of Housing	76
A.4 Bottom View of Housing	77
A.5 Cross Sectional View of Housing	78
A.6 Cover of Housing	79
APPENDIX B: ADDITIONAL RESULTS	80
B.1 RRV Soil BRF	80
B.2 Signal from Spectralon Panel	80
B.3 Signal from RRV soil	81
B.4 Radiometric Calibration Comparison	81
REFERENCES	82

List of Figures

Fig. 1: Walk paths for different sensor overpasses at Railroad Valley, Nevada.	13
Fig. 2: Remote Sensing Group member recording a reference panel measurement with ASD (left) and walking Railroad Valley with an ASD and recording ground measurements (right).	14
Fig. 3: Automated solar radiometer used to take atmospheric measurements.	15
Fig. 4: Satellite image of Railroad Valley playa. Purple box represents the 1km x 1km area and location of RadCaTS in Railroad Valley, Nevada.	16
Fig. 5: GVR equipped with linear motion (Top Right), stationary GVRs (Top Left), Cimel sun photometer (Bottom).	17
Fig. 6: ASD hyperspectral surface BRF (orange line) fit over the GVR multispectral BRF.	18
Fig. 7: SpAM. Photo taken during SpAM deployment.	19
Fig. 8: Zemax design of SpAM's optical layout.	19
Fig. 9: SpAM full field of view of 7.15° , represented by red shaded region, equates to a length of approximately 75 cm and a minimal width.	20
Fig. 10: Spectral sensitivity and spectral resolution for the C12880MA.	24
Fig. 11: Optical layout of the C12880MA.	25
Fig. 12: C12880MA temperature dependence with dark readings.	26
Fig. 13: Components in the C13016 evaluation, including the sensor board, connection cable, and evaluation board. Also shown is the micro-spectrometer.	27
Fig. 14: Assembled evaluation circuit.	28
Fig. 15: GUI screenshot that includes an arbitrary measurement.	29
Fig. 16: Parameter settings available in the evaluation software GUI.	30
Fig. 17: Calibration coefficients provided by the manufacturer for the pixel to wavelength conversion.	31
Fig. 18: 3D model: front view (top left), cover (top right), bottom front view (bottom left), aerial view (bottom right).	36
Fig. 19: SOLIDWORKS models of the evaluation board and sensor board.	37
Fig. 20: Final printed housing with cover.	39
Fig. 21: Housing with integrated evaluation circuit.	40
Fig. 22: ASD spectroradiometer and micro-spectrometer set up in front of the SIS to view same target area for radiometric calibration.	42
Fig. 23: Setup for making measurements with panels. The setup shown here is for measuring the Spectralon panel. The same setup is used to measure the 48 % panel.	43
Fig. 24: FOV test setup. Spectrometer is traversed from the edge of the black panel to Spectralon panel in both x direction and y direction. Note: panel resting on spectrometer provides shade to the plastic and electronics during downtime and is not present during testing.	44
Fig. 25: Setup for optimal integration time characterization. Measurements are made of the Spectralon panel and RRV soil. The instrument is positioned such that only the surface of interest is within the FOV.	45
Fig. 26: Test setup for SNR measurements. The micro-spectrometer is centered with the output aperture of the SIS.	46
Fig. 27: Testing setup for measuring the responsivity dependence on temperature.	47
Fig. 28: Lollipop test setup for the micro-spectrometer.	49
Fig. 29: Laboratory setup for spectral characterization. Left picture is a top view of the setup, spectrometer is centered in the sphere aperture and the laser is positioned to send an unobstructed beam into the SIS. Right picture shows the green laser illuminating sphere. The red laser is substituted for the green laser during the 633 nm measurement.	50
Fig. 30: The setup for measuring the surface reflectance of asphalt. The same setup is used for other surface measurements.	51
Fig. 31: Linearity evaluation for different radiance levels. The dark corrected signals for each wavelength are plotted versus the relative radiance.	54

Fig. 32: Linearity evaluation for various integration times. The dark corrected signals for each wavelength are plotted versus the integration time used during measurement.	55
Fig. 33: Linearity evaluation using Spectralon panel and 48 % reflective panel. Top graph shows the dark corrected DNs of the two panels measured with the micro-spectrometer. Bottom graph shows the ratio of the measured DNs, and the ratio between the laboratory measured BRDF for the panels. The measurements are taken at a SZA of 45°. Purple marker points are the wavelengths for which calibration measurements are taken at, orange is the interpolation of these values onto the micro-spectrometer's spectrum.	57
Fig. 34: SNR vs wavelength for 3 different sources.	59
Fig. 35: Temperature dependence for the system responsivity for specific wavelengths. A linear fit is performed on the measurements.	61
Fig. 36: Percent difference of measurement from the ambient measurement (25.7 °C).....	61
Fig. 37: Stray light characterization as a function of distance from the lollipop.....	62
Fig. 38: Spectral characterization of the micro-spectrometer for a 543 nm and 633 nm lasers for a 100 ms.....	63
Fig. 39: Spectral characterization plotted on a log scale to observe the out of band response by the C12880MA	63
Fig. 40: Percent difference in micro-spectrometer output of data taken on 12 August 2021 and 30 September 2021.....	64
Fig. 41: Reflectance measurements for asphalt and grass surfaces. The black curves represent reflectance measurements taken with the C12880MA.....	65
Fig. 42: Calibration coefficients for the micro-spectrometer for each radiometric calibration.....	66

List of Tables

Table 1: Comparison between ESD safe 3D printing filament vs standard 3D printing filament with ESD safe coating.....	34
Table 2: Comparison specifications between ESD PLA and ESD ABS, both manufactured by 3DXTECH.....	35
Table 3: Lead time and cost comparison between two material options.....	39
Table 4: Linearity percent error from linear fit of the micro-spectrometer for different radiance levels.	55
Table 5: Linearity percent error from linear fit of the micro-spectrometer for different integration times.....	56
Table 6: SNR values for specific wavelength channels from different sources.....	59
Table 7: Dark reading SNR for 550.9 nm channel over a span of 36 hours and 29 minutes. Measurements shown are taken using dark mode in the system GUI.	60

Abstract

The Remote Sensing Group (RSG) of the Wyant College of Optical Sciences at the University of Arizona currently has a single hyperspectral instrument, a Spectrometer Arduino Mega (SpAM), deployed to its Radiometric Calibration Test Site (RadCaTS). Results have shown SpAM to be a robust and accurate instrument, however its high degree of customization makes it difficult to productively reproduce. The Hamamatsu C12880MA is a commercial micro-spectrometer that may provide a solution to RSG's need for an easily deployable and reproducible hyperspectral instrument. The C12880MA is an ultra-compact grating-based spectrometer that operates in the visible and near-infrared (VNIR).

This work presents the initial development of the C12880MA, which involves prototyping and characterizing the device for automated field deployment. The micro-spectrometer is prototyped using a device-specific evaluation circuit, measurement software, and a custom 3D printed electrostatic discharge (ESD) safe housing. It is characterized in RSG's laboratory and auxiliary facilities. The eventual goal for this device is to become an autonomous standalone system that can be easily deployed and integrated into the RadCaTS suite of instruments. The results from this work will determine the efficacy of the instrument as well as its potential for future deployment. The daily hyperspectral measurements from this device, if deployed, will supplement the current data, and reduce the uncertainty of RadCaTS results.

Chapter 1: Introduction

1.1 Overview of Thesis

This work presents the development of a commercial micro-spectrometer for possible future deployment and integration into the Remote Sensing Group's Radiometric Calibration Test Site. The development of such an instrument is motivated by the prospect of it being easily deployable, integrable, and reproducible. Additionally, the micro-spectrometer provides a cost effective and robust solution to RSG's need for continuous hyperspectral measurements at RadCaTS throughout the day.

Chapter 1 provides a brief discussion on the background of the Remote Sensing Group, including high-level details on its field work and research facilities. Further, Chapter 1 presents information on the reflectance-based vicarious approach that RSG employs for the post-launch radiometric calibration of airborne and spaceborne sensors. Chapter 1 also explains the architecture of RSG's automated calibration test site, RadCaTS. Lastly, Chapter 1 describes the Spectrometer Arduino Mega, which is a field deployed automated hyperspectral instrument developed by a previous RSG MS student.

Chapter 2 presents the requirements that the micro-spectrometer must satisfy to be a candidate for remote field deployment. This includes a discussion on the optical, electrical, and mechanical parameters that current deployed systems meet and how those relate to the development of a new instrument. Chapter 2 then introduces the micro-spectrometer chosen for potential deployment. Chapter 2 also describes the micro-spectrometer's manufacturer given optical, electrical, and mechanical specifications.

Chapter 3 describes the prototyping phase for this micro-spectrometer. The chapter describes the evaluation circuit and evaluation software used to operate the

micro-spectrometer. Chapter 3 provides a discussion of the design process behind the housing for the micro-spectrometer. Additionally, Chapter 3 presents the fully integrated prototype.

Chapter 4 presents the laboratory characterization of the micro-spectrometer. The characterization consists of detector linearity, field of view (FOV), optimal integration times, signal to noise ratio (SNR), dark measurement noise, temperature dependence, stray light, spectral resolution, repeatability, and surface reflectance retrieval measurements. Similarly, Chapter 4 describes the objectives and test bed for each of these characterizations. The chapter also presents the absolute radiometric calibration for the micro-spectrometer.

Chapter 5 presents the processed results from the raw data collected during the laboratory characterization. The chapter describes the data processing procedures and summarizes the results for each characterization. Chapter 5 includes data from both the characterization measurements and radiometric calibration.

Chapter 6 concludes the work presented in this thesis. Chapter 6 provides an analysis of the processed results and includes a discussion on the implications of the micro-spectrometer's characterization on its potential field deployment. Chapter 6 also presents the future work with this micro-spectrometer and a recommendation on the integration for this device into the RadCaTS suite of instruments.

1.2 Remote Sensing Group

1.2.1 Background

The Remote Sensing Group of the Wyant College of Optical Sciences focuses its research on the pre- and post-launch calibration of Earth-observing sensors that operate

in the solar-reflective regime (400 nm to 2500 nm). Since its inception in the mid-1980s, RSG has collected data and performed ground-based vicarious calibrations at multiple locations across the United States [1]. RSG has historically used the reflectance-based approach for the ground-based radiometric calibration of in-flight sensors. The reflectance-based approach yields an uncertainty of about ± 2 % [2]. Currently, RSG primarily uses one site for data collection, which is Railroad Valley (RRV), Nevada [3]. In 2004, RSG began the development of RadCaTS, an automated and unmanned calibration approach, at RRV [4]. Since then, RSG has focused more on automating the measurements used in the ground-based vicarious radiometric calibration of in-flight airborne and spaceborne satellite sensors as well as on improving the RadCaTS results. As a companion to its field work, RSG developed a state-of-the-art laboratory for custom instrument fabrication and for the calibration of support instruments.

1.2.2 Ground-Based Vicarious Radiometric Calibration

Earth-observing sensors typically go through two main phases of calibration known as pre-launch and post-launch. A pre-launch calibration is conducted in a controlled laboratory setting, while the post-launch calibration uses onboard and ground-based systems for calibration [3, 5]. Monitoring the post-launch radiometric calibration is important for long-term trending as it may impact the quality of science products produced using these instruments [6]. Prior to the development of RadCaTS, RSG primarily employed the reflectance-based vicarious calibration technique for its radiometric calibration work. The value of the vicarious calibration technique is that it relies on data that is entirely independent of any onboard sensor or calibration systems [2]. The reflectance-based approach utilizes in situ measurements of surface reflectance and

atmospheric transmission as inputs into a radiative transfer code [7]. The code predicts the top-of-atmosphere (TOA) quantity for the sensor of interest, which is then compared to the value measured by the sensor itself. This approach has been implemented by RSG for over 35 years and currently yields an uncertainty on the order of $\pm 2.5\%$ [2].

Traditionally for the reflectance-based radiometric calibration, the surface reflectance is measured using a portable hyperspectral spectroradiometer, which is carried by an operator in a predetermined pattern for a given test site. RSG currently uses the newest Analytical Spectral Devices (ASD) FieldSpec 4 spectroradiometer for its field work. The spectroradiometer has a wavelength region of 350 nm to 2500 nm and is sampled to a 1 nm resolution using software provided by the manufacturer.

Measurements are taken of the surface in digital numbers (DN) intermittently at predetermined points along the designated walk path (Fig. 1). RSG typically uses an 8° full field of view (FFOV) foreoptic on the ASD for measurements. The foreoptic of the ASD is attached to a boom arm during operation to ensure that shadows from the operator do not impede on the FFOV of the spectroradiometer. An example is shown in Fig. 2.

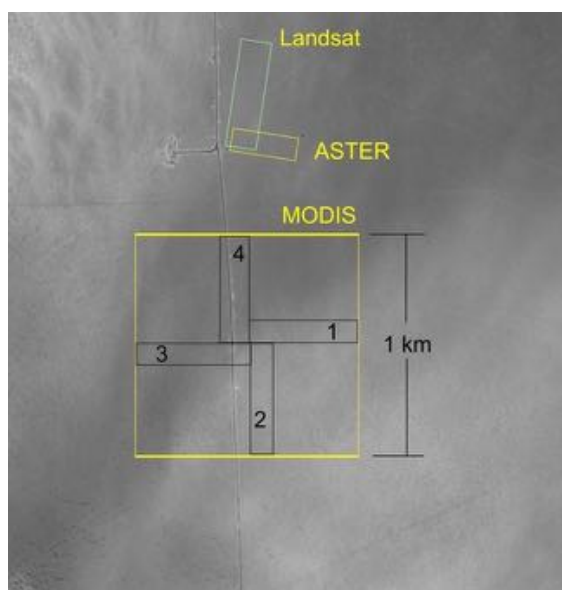


Fig. 1: Walk paths for different sensor overpasses at Railroad Valley, Nevada.

Prior to, during, and after walking the site, DN measurements are also made of a reference Spectralon panel. The reference Spectralon panels are routinely measured in RSG's laboratory to characterize their bidirectional reflectance factor (BRF) as a function of angle and wavelength [8]. The raw measurements and the panel BRF are used to determine the surface reflectance, $\rho_{surface}$, of the site through the ratio:

$$\rho_{surface} = \rho_{panel} \frac{DN_{surface}}{DN_{panel}}$$

Eq. 1

where ρ_{panel} is the BRF of the reference Spectralon panel, $DN_{surface}$ is the digital number measured by the ASD of the surface, and DN_{panel} is the digital number measured by the ASD of the reference spectralon panel. The BRF of the test site surface is averaged over all measurements and is a spectral quantity from 350 nm to 2500 nm with a 1 nm resolution [3].



Fig. 2: Remote Sensing Group member recording a reference panel measurement with ASD (left) and walking Railroad Valley with an ASD and recording ground measurements (right).

Atmospheric transmission measurements are taken in tandem with the surface reflectance measurement. The atmospheric transmission is determined using measurements from an on-site automated solar radiometer (ASR) [9] and an on-site meteorological station. The ASR, Fig. 3, measures the incoming solar irradiance

extinction due to atmospheric absorption and scattering, while the metrological station measures the pressure and temperature of the site during a sensor overpass.



Fig. 3: Automated solar radiometer used to take atmospheric measurements.

The surface reflectance and atmospheric measurements are used as inputs into the MODerate resolution atmospheric TRANsmission (MODTRAN) radiative transfer code to predict the TOA spectral radiance at a specific time for a sensor under test. MODTRAN was developed by, and is currently maintained by the United States Air Force Research Lab (AFRL) [7].

1.2.3 Radiometric Calibration Test Site

While the conventional reflectance-based radiometric calibration approach is an accurate and well-understood calibration technique, there are a few drawbacks. Notably, the number of possible calibrations is restricted due to the time, cost, and conditions of getting personnel on site during a sensor overpass [10]. Due to this limitation, RSG began the development of the Radiometric Calibration Test Site in 2004 at Railroad Valley, Nevada. RadCaTS is an automated approach to the reflectance-based vicarious radiometric calibration.



Fig. 4: Satellite image of Railroad Valley playa. Purple box represents the 1km x 1km area and location of RadCaTS in Railroad Valley, Nevada.

RadCaTS is similar to the reflectance-based approach, but there are few minor changes in the data collection process. Surface reflectance measurements are taken using custom designed and fabricated multispectral ground-viewing radiometers (GVRs), and atmospheric measurements are collected using a Cimel CE-318T sun photometer [11].

There are currently six nadir-viewing stationary GVRs and one nadir-viewing GVR equipped with linear motion deployed to RadCaTS (Fig. 5). A GVR consists of 8 spectral channels, each with a 20 nm spectral resolution (full width at half maximum, (FWHM)). The center wavelengths for each of the eight channels are 400 nm, 450 nm, 500 nm, 550 nm, 650 nm, 850 nm, 1000 nm, and 1550 nm.



Fig. 5: GVR equipped with linear motion (Top Right), stationary GVRs (Top Left), Cimel sun photometer (Bottom).

GVRs are absolutely radiometrically calibrated using a 1 m spherical integrating source (SIS) and a calibrated transfer radiometer [2]. The surface BRF at each GVR channel is determined using the absolute radiometric calibration. The BRF for a GVR measurement is determined by

$$\rho_{surface} = \frac{\pi C_{GVR} V_{GVR}}{\frac{E_0}{d^2} \tau_A \cos\theta + E_{sky}}$$

Eq. 2

where C_{GVR} is the calibration coefficient with units of $[\frac{W}{V \cdot m^2 \cdot \mu m \cdot sr}]$, V_{GVR} is the radiometer output in Volts, E_0 is the exoatmospheric spectral irradiance $[\frac{W \cdot AU}{m^2 \cdot \mu m}]$, d is the normalized Earth-Sun distance in Astronomical Units $[AU]$, τ_A is the direct solar beam transmission

[unitless], θ is the solar zenith angle, and E_{sky} is the diffuse spectral sky irradiance

$$\left[\frac{W}{m^2 \cdot \mu m}\right].$$

While the details of the radiative transfer code are not imperative to the scope of this work, it must be acknowledged that the code requires a surface BRF with a 1 nm spectral resolution. Using a library of ASD measurements collected by RSG personnel over the past 30 years at RRV, the averaged multispectral surface BRF measured with the GVRs is matched to a best fit ASD surface BRF measurement. The best fit ASD BRF measurement is selected autonomously using the RadCaTS processing code. Fig. 6 presents an example of the GVR measured multispectral BRF fit with an ASD hyperspectral BRF.

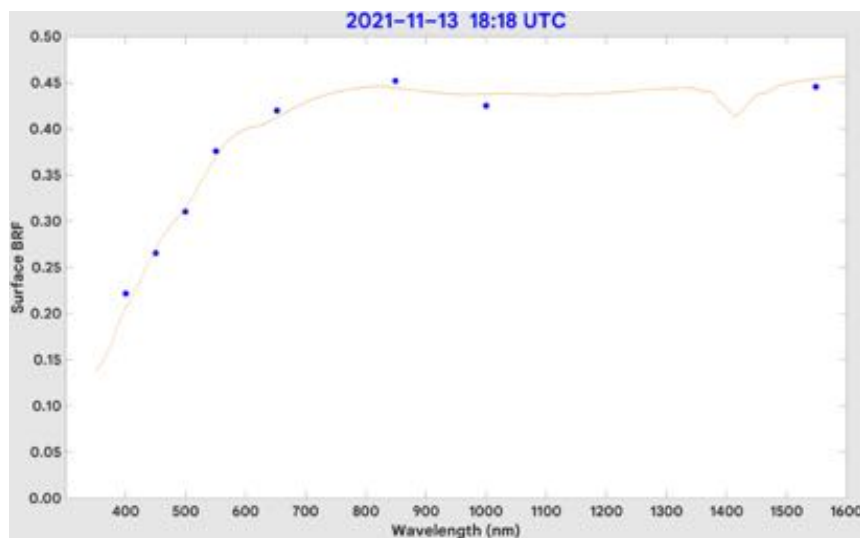


Fig. 6: ASD hyperspectral surface BRF (orange line) fit over the GVR multispectral BRF.

The best fit hyperspectral data and Cimel sun photometer atmospheric data become the inputs into MODTRAN to calculate the TOA spectral radiance.

1.3 Spectrometer Mega Arduino

SpAM, deployed in Spring 2019, is RSG's low budget, stand alone, automated prism spectrometer that has an operating wavelength region of 433 nm to 767 nm with a

spectral resolution of approximately 2 nm [12]. SpAM, shown in Fig. 7, provides RSG with an automated approach to collecting daily hyperspectral measurements. Prior to the deployment of SpAM, in situ ASD measurements were RSG's only source of hyperspectral data of the RRV surface. Persistent hyperspectral data at RRV allows RSG to better characterize the RRV surface and reduce the uncertainty in RadCaTS results.



Fig. 7: SpAM. Photo taken during SpAM deployment.

Similar to a GVR, SpAM is absolutely radiometrically calibrated and designed to measure surface reflected radiance. The optical layout of SpAM consists of a 40 μm entrance slit, a collimation lens, a dispersive prism, and a linear CMOS array (Fig. 8).

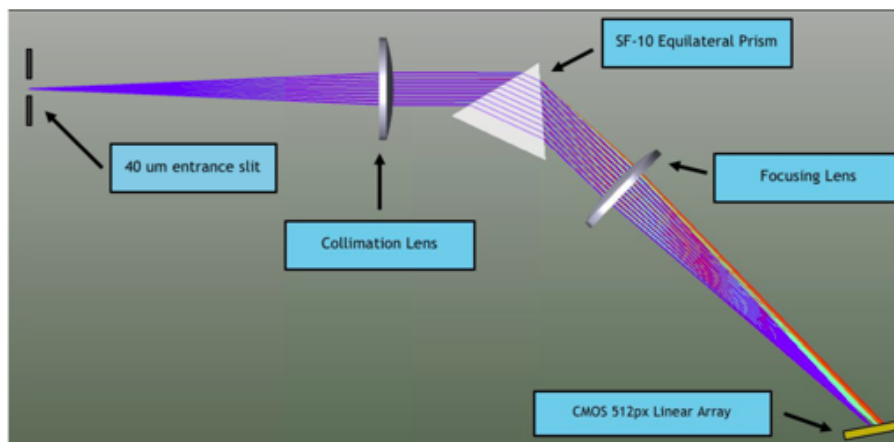


Fig. 8: Zemax design of SpAM's optical layout.

The data acquisition system of SpAM is based on a Mega Arduino Microcontroller and data are currently stored directly on a micro-SD card. SpAM is developed for integration into the wireless satellite uplink system at RadCaTS, but currently, data are manually downloaded during maintenance trips to RRV. SpAM is outfitted with a durable and weatherproofed housing to withstand the harsh environmental conditions at RRV. The initial post-deployment analysis of SpAM's surface measurements indicated that measurement uncertainty is on the order of $\pm 4\%$, when compared to GVR surface measurements [13].

While SpAM is robust instrument that yields accurate results, it does have limitations. Many of the parts incorporated in SpAM are uniquely customized or configured from their commercial state [13], making it difficult to productively and accurately reproduce the current working design onto multiple instruments.



Fig. 9: SpAM full field of view of 7.15° , represented by red shaded region, equates to a length of approximately 75 cm and a minimal width.

Further, SpAM has a limited FOV (Fig. 9). Consequently, the reduced spatial sampling size may not provide an accurate representation of the RRV surface cracks, dips, and mounds [14]. RSG would need to either deploy an array of SpAM instruments

or raise the instrument higher above the ground to increase the spatial sampling of the instrument. However, deploying multiple instruments is unfavorable due to SpAM's customization, and raising the instrument is an impractical solution as RRV is a designated low-altitude flight zone. In addition, the mounting assembly, while robust, is large and not the most efficient setup. Fig. 7 illustrates the complexity of SpAM's mounting assembly. There are four in-ground steel fence posts, two crossed 45° aluminum beams for stability, two aluminum beams for mounting SpAM, and additional beams that connect the in-ground posts for increased stability. The micro-spectrometer described in this thesis is a more efficient system in terms of deployment to RadCaTS and mass reproduction.

Chapter 2: Device Description

Multiple deployed hyperspectral instruments will provide greater spatial sampling of the RRV surface and also reduce the uncertainty in RadCaTS results by filling in the spectral regions between GVR channels in the visible spectrum. The difficulty in a consistent and efficient reproduction of SpAM prompted RSG to pursue a commercial spectrometer with a greater ease of mass reproducibility. This chapter presents the requirements a new spectrometer must maintain in order to be a potential candidate for field deployment. The chapter then presents the chosen spectrometer, the Hamamatsu C12880MA, and the instrument specifications provided by the manufacturer. The spectrometer discussed in this work is a proof of concept for future integration.

2.1 Requirements

The spectral characteristics of SpAM provide a model for the new spectrometer. SpAM operates from 433 nm to 767 nm, which covers approximately half of the spectral region covered by the eight GVR channels. RSG designed SpAM to have a spectral resolution less than the 20 nm (FWHM) resolution relative spectral response (RSR) of a given GVR channel. SpAM currently measures a spectral resolution of approximately 2 nm [12]. Unfavorably, SpAM has a varied spectral sampling interval due to the nonlinear dispersive nature of prisms. A spectrometer with a constant or near-constant spectral sampling interval in the VNIR would simplify the spectral calibration and data processing.

The spectrometer must also align with certain optical parameters to be a potential candidate for deployment. First off, the spectrometer should have a FOV that allows for an accurate representation of the RRV surface [14]. The instrument, like the other deployed radiometers, also needs to have linear responsivity per wavelength with

changes to the input light level. Additionally, the SNR of the spectrometer should be large enough to meet the surface reflectance uncertainty specification of RadCaTS, 4 % [15]. As a reference, the SNR of GVR 22 and GVR 23 ranges from 1500 to 7200, based on wavelength [2], greatly exceeding the requirement. Lastly, the spectrometer must have limited and/or correctable stray light characteristics. Large amounts of uncorrected stray light will degrade the quality of data during deployment as the spectrometer would see both shadows and reflections of itself.

The spectrometer additionally must operate as a standalone instrument for field deployment. This includes being able to withstand harsh weather conditions, run on its own power supply system, and be programmed for autonomous data collection. The RRV site experiences temperatures typically ranging from -20°C to 45°C throughout the year, and weather conditions occasionally include high winds, dust storms, and snowstorms. The spectrometer must be able to withstand these conditions. RadCaTS, where RSG deploys its autonomous instruments at RRV, is an off-grid location, which means that the spectrometer must run on its own power supply system. The spectrometer also needs to be programmable for autonomous data collection to provide RadCaTS and RSG with persistent hyperspectral data throughout the day. The GVRs currently deployed at RadCaTS collect data every two minutes and a similar temporal data collection timeframe is anticipated for the new spectrometer.

Lastly, the new spectrometer must be easily reproducible and integrable in a remote field environment. The main drawback of SpAM is its customization, which makes it difficult to reproduce in a productive and precise manner. The design of the new spectrometer needs to be as simple as possible so that RSG can deploy multiple

instruments efficiently. Furthermore, the spectrometer must be able to connect and communicate with the satellite uplink base station at RRV, which is used to upload daily data to the University of Arizona. This will allow RSG incorporate daily data from the spectrometer into the processing scheme that determines the surface reflectance for a given time of interest.

2.2 Description of Device

The C12880MA is a micro-spectrometer designed and manufactured by Hamamatsu. It has dimensions of 20.1 mm × 12.5 mm × 10.1 mm, and a weight of 5 g. The micro-spectrometer has a spectral range of 322 nm to 888 nm. It uses a high sensitivity linear CMOS image sensor. The sensor consists of 288 14 μm × 200 μm pixels. The spectral response and spectral resolution for the C12880MA are shown in Fig. 10. The micro-spectrometer is most sensitive between 400 nm and 600 nm, while the spectral resolution ranges between 8 nm and 11 nm for a given wavelength.

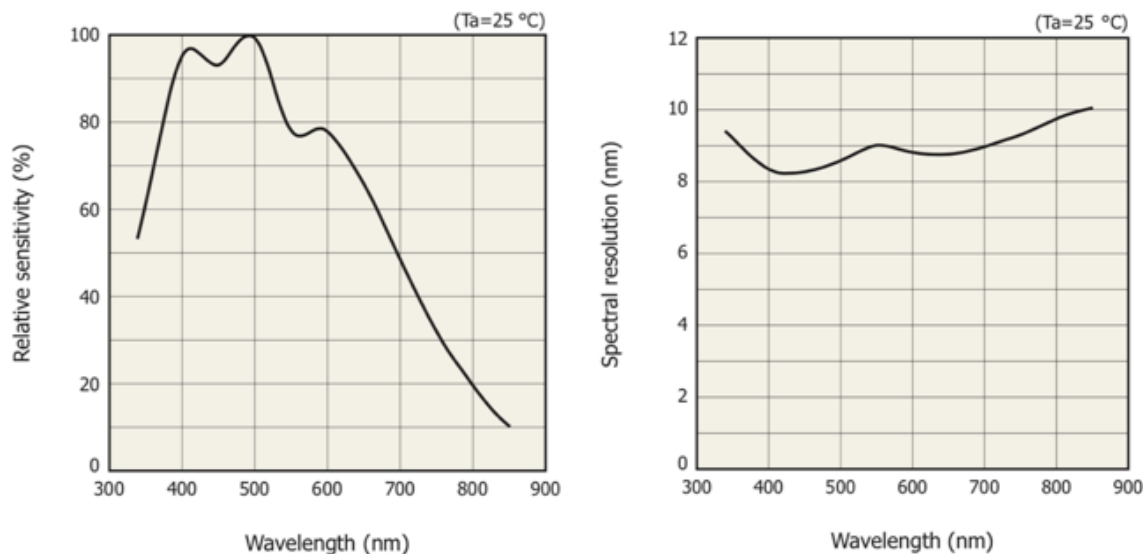


Fig. 10: Spectral sensitivity and spectral resolution for the C12880MA.

The C12880MA is a diffraction grating based spectrometer. The optical layout consists of a 50 μm × 500 μm input slit, a reflective concave blazed grating, and a linear

CMOS sensor (Fig. 11). The design yields a numerical aperture of 0.22. The grating is a multifunctional component that disperses the light and concurrently focuses the dispersed light onto the sensor. A secondary benefit of the diffraction grating is that light is dispersed linearly.

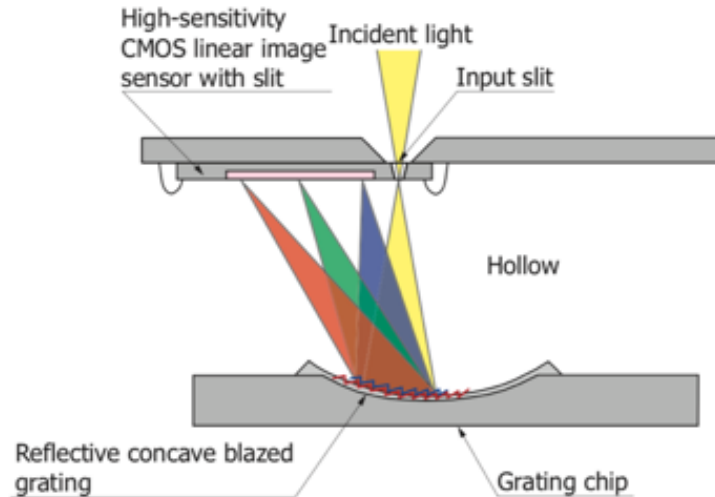


Fig. 11: Optical layout of the C12880MA.

The C12880MA requires a supply voltage between -0.3 V and 6 V for operation, however the most efficient operation supply voltage is between 4.75 V and 5.25 V. The micro-spectrometer operates between 5 °C and 50 °C, and has a user-specified storage temperature range of -20 °C to 70 °C. The system responsivity is temperature dependent, the DN output is directly related to the sensor temperature and there is an exponential impact of temperature effects on the detector output after 35 °C (Fig. 12). The dark output voltage for the micro-spectrometer is around 0.8 mV, and saturation occurs at 4.3 V. The micro-spectrometer includes contact points for connections to a power supply and a trigger input.

■ Dark output vs. ambient temperature (typical example)

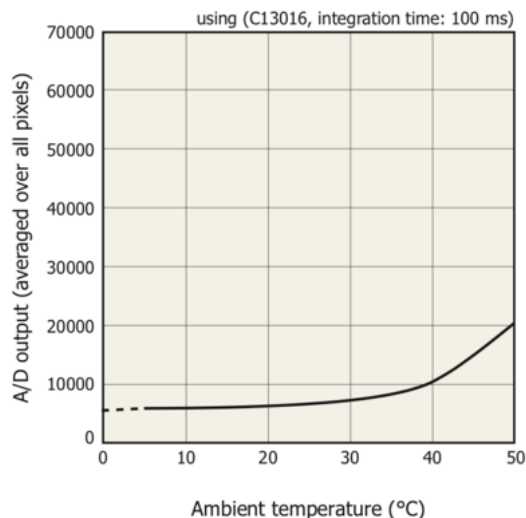


Fig. 12: C12880MA temperature dependence with dark readings.

The C12880MA satisfies the requirements for a new autonomous hyperspectral field instrument for RadCaTS. Its design is relatively simple, it has a hyperspectral detector, and it is compact enough to integrate into either its own system or into another. The spectral range includes the VNIR. The spectral resolution is less than 20 nm, and the spectral sampling interval should be relatively constant. The FOV is large enough to provide spatial sampling similar to that of the GVRs as well as the portable spectroradiometers historically used to collect surface reflectance data. Furthermore, the temperature specifications of the C12880MA are appropriate for use at RRV. It also uses a low operating voltage and has direct integration capabilities for autonomous operation at a remote site.

Chapter 3: Prototyping

The Hamamatsu C12880MA micro-spectrometer requires some form of prototyping and integration for operation. This chapter focuses on the prototyping and integration of the micro-spectrometer. The micro-spectrometer is integrated with an evaluation circuit that includes a plug and play measurement software. The micro-spectrometer is converted into a robust test instrument through a custom designed instrument-specific 3D printed housing. Field deployment implications are also considered during the prototyping.

3.1 Hamamatsu Evaluation Circuit

3.1.1 Components

Hamamatsu provides a C13016 evaluation circuit in conjunction with the C12880MA. The C13016 evaluation circuit is designed to directly evaluate the incident light on the micro-spectrometer's sensor board at a 16 bit level. Shown in Fig. 13, there are three components in the evaluation circuit: a sensor board, a board-to-board connection cable, and lastly the evaluation board.



Fig. 13: Components in the C13016 evaluation, including the sensor board, connection cable, and evaluation board. Also shown is the micro-spectrometer.

Fig. 14 displays the connected circuit. The micro-spectrometer is coupled with the sensor board, which is connected to the evaluation board via the connection cable. The sensor board receives electrical signals from the micro-spectrometer's CMOS sensor and transmits them to the evaluation board through the connection cable. The evaluation board converts the signals to DNs on a 16 bit scale and transmits them to a personal computer (PC).



Fig. 14: Assembled evaluation circuit.

The C13016 evaluation board includes a USB 2.0 port for power and communication with a PC. The board also allows for a trigger input through the BNC connector, which accepts inputs between 0 V and 6 V.

3.1.2 Evaluation Software

Moreover, the C13016 evaluation board also comes with evaluation software. The evaluation software has the option to use either a graphical user interface (GUI) version for simple plug and play use or a Visual Studio development code for customization.

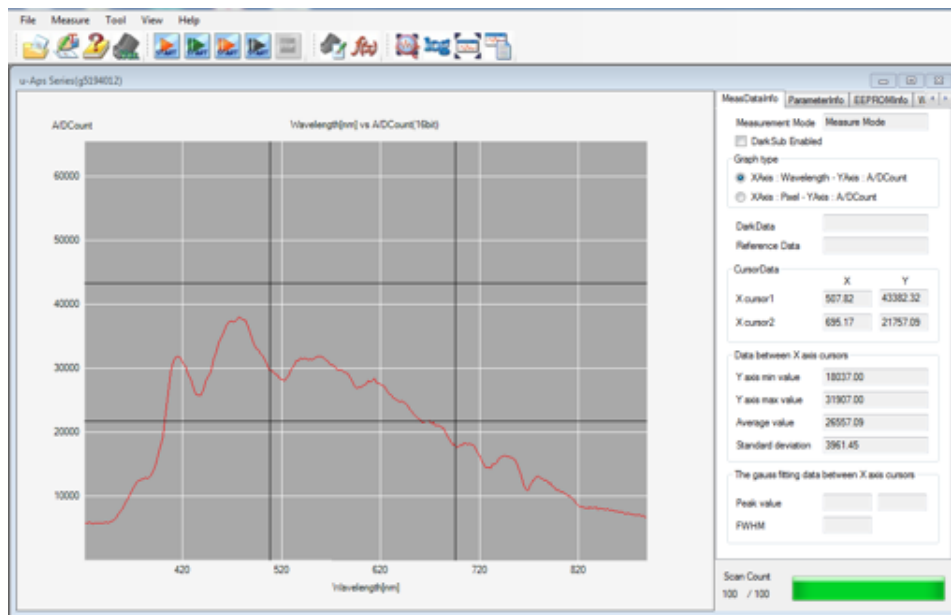


Fig. 15: GUI screenshot that includes an arbitrary measurement.

The GUI provides an initial evaluation method that is effective for preliminary testing and characterization (Fig. 15). In the GUI, there are six different parameters a user can configure: scan count, average count, integration time, capture mode, trigger polarity, and trigger output (Fig. 16). Scan count and average count define the measurement settings, while integration time, capture mode, trigger polarity, and trigger output define the spectrometer settings. Scan count is the number of measurements recorded during one measurement, and it can range from 1 to 5000. Average count is the number of measurements averaged per scan, and it can be set from 1 to 255. The average count and scan count can be related to each other and to the total number of measurements by Eq. 3.

$$Average_{count} * Scan_{count} = Total_{count}$$

Eq. 3

Integration time defines the amount of time the CMOS detector of the C12880MA collects photons, and it ranges from 11 μ s to 1 s, with 1 μ s steps. Capture mode defines the type of capture, which is either by a trigger input or a specified number. The trigger polarity is

the edge, rising or falling, that a trigger input is read on. Lastly, the trigger output setting defines another trigger option that can also start the measurement. The trigger output can only be used in the specified number capture mode.

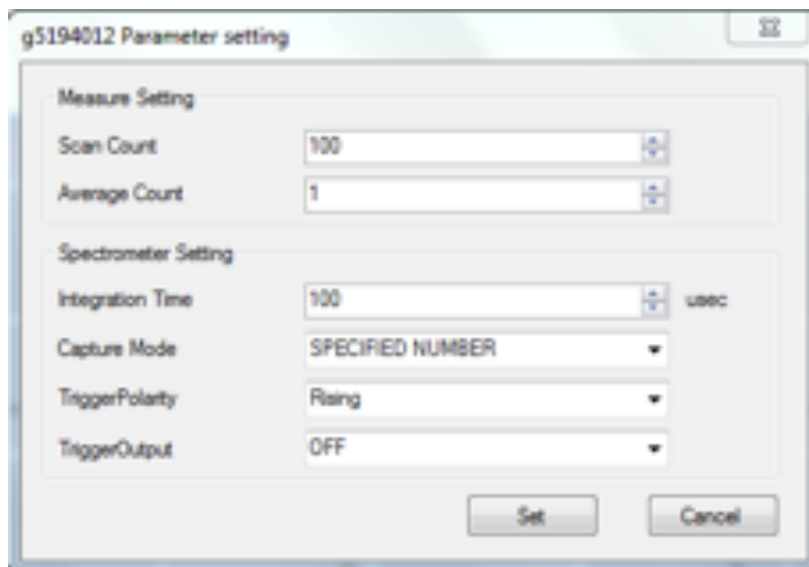


Fig. 16: Parameter settings available in the evaluation software GUI.

There are four different measurement modes in the evaluation software: dark mode, monitor mode, measure mode, and reference mode. It should be noted that the dark mode and measure mode perform the same physical measurement operation set by the measurement and spectrometer settings. The difference between the two is file allocation. Dark mode is used to acquire a dark reading. The software stores a separate dark dataset after completion of a dark measurement. Measure mode is used to record and store a measurement dataset. Reference mode is used to record a reference dataset, the software stores a reference file after completion of a measurement and can call on it during any future measurement. Monitor mode is similar to the measure mode but has no scan count limit and does not store any data, it is simply a live stream of the output signal from the C12880MA. The four modes are given by the four play buttons along the toolbar

in the GUI (Fig. 15): monitor, reference, measure, and dark, in order from left to right. Measurements can be made as DN versus pixel number or DN versus wavelength in nm.

The C12880MA has already been spectrally calibrated (pixel to wavelength) by the manufacturer. Conversion from pixel to wavelength takes place within the evaluation software and is given by the quintic equation,

$$Wavelength [nm] = A0 + B1 * x + B2 * pix^2 + B3 * x^3 + B4 * x^4 + B5 * x^5 \quad Eq. 4$$

where A0, B1, B2, B3, B4, and B5 are all calibration coefficients for the pixel to wavelength conversion, and x is the pixel number along the linear CMOS array. The values for each coefficient are shown in Fig. 17. The software provides the freedom to configure these coefficients if a recalibration is required, or if there is discrepancy between the manufacturer-provided calibration coefficients and the ones preloaded into the software.

Wavelength conversion coefficients	
A0	3.177680273E+002
B1	2.700686029E+000
B2	-1.144517407E-003
B3	-8.530887275E-006
B4	1.496279381E-008
B5	-5.706326871E-012

Fig. 17: Calibration coefficients provided by the manufacturer for the pixel to wavelength conversion.

The GUI allows the user to save all measurement data and settings for future use. Measurement data, which includes measure mode, dark mode, and reference mode measurements, are all stored as independent comma-separated value (CSV) files.

Meanwhile, the device settings, which include instrument information, date and time, calibration coefficients, and parameter settings, are stored in a separate text file.

Along with the GUI, Hamamatsu provides a sample application and developer tools through Visual Basic and Visual C++. The basic sample code is essentially an extension of the GUI. The main difference between the two is that while the GUI is limited in its functionality and customization, the sample application can be further developed for application-specific functions. There are a series of dynamic link library (DLL) functions provided by Hamamatsu that can be integrated into the sample application for customization. The flexibility within the sample application is key for the long-term development of this instrument. Although the GUI is a great tool for laboratory characterization, it has no functionality in a field deployment setting. The sample application, on the other hand, has the potential to develop the micro-spectrometer into an automated system that can be deployed and integrated into RadCaTS.

3.2 Housing

3.2.1 Reasons for Housing

The secondary element of the prototyping phase is to design and fabricate a housing for the micro-spectrometer and its evaluation circuit. The bare evaluation circuit (Fig. 14) lacks stability and rigidity for robust testing, specifically in the connection cable. Even if a makeshift setup is constructed, the spectrometer does not stay in a fixed position over a long period of time due to the instability of the connection cable. Furthermore, the bare circuit does not allow for measurements to be made in multiple orientations as there is only one configuration to secure the evaluation board down on an optical bench. These

issues make it necessary to design an instrument-specific housing that converts the bare circuit into a robust testing device that is easy to setup and use in different environments.

Additionally, being an ESD-susceptible device, the bare circuit can only be used in ESD-safe settings. The requirement of an ESD-safe environment limits the number of potential testing environments with the bare circuit. While it is possible to create a makeshift ESD-safe test bed using an ESD mat or other ESD safe practices, the test setup becomes overly complicated and inefficient. Thus, the housing must provide and maintain an ESD-safe environment for the evaluation circuit without increasing the complexity of the test setup.

Lastly, a housing is needed for general storage and protection. Any form of housing is beneficial to protect the electronics from dust, dirt, and sun exposure. Similarly, a housing reduces the impact to the electronics caused by general wear and tear, accidental drops, and other unpredictable mishaps.

3.2.2 Design Process

The housing design process takes the functionality, cost, performance, and lead time into consideration. The main objectives of the housing design are to transform the micro-spectrometer and evaluation circuit into a simple and robust testing device, provide an ESD-safe environment for the electronics, and protect the electronics from general wear and tear.

The design of the housing must induce rigidity into the evaluation board, sensor board, and connection cable and also must hold the micro-spectrometer stable and optically aligned. Furthermore, it is essential for the housing to be rigid, yet adaptable. A

versatile housing will allow the spectrometer to be used in various testing environments. The final housing should also allow for a simple and efficient setup process.

The simplest method for constructing the housing, while satisfying the design conditions, is to 3D print the housing. Various holes, slits, and offsets are necessary additions on the faces of the housing to accommodate the different features of the evaluation and sensor board. These types of cuts are time consuming and difficult to construct using classical machining techniques. 3D printing, in contrast, can easily route the incisions and contours with great precision. Additionally, 3D printing provides a cost-effective and minimal lead time solution in comparison to a classical machining technique.

In addition to being robust and adaptable, the housing must be ESD safe as the electronics and micro-spectrometer are all susceptible to electrostatic discharge. A suitable housing would essentially place the electronics in an ESD-safe bubble and the instrument could then be used in many testing environments. A material is considered ESD safe if it measures a surface resistivity between 10^6 and $10^9 \Omega$. Since the housing is to be 3D printed, the materials available for use are restricted to 3D printing filaments. Two design options are taken into consideration to produce an ESD-safe housing, directly using a premade ESD-safe 3D printing filament or applying an ESD-safe paint coating onto a standard 3D printing filament.

Table 1: Comparison between ESD safe 3D printing filament vs standard 3D printing filament with ESD safe coating.

	ESD-Safe Material*	Standard Material* w/ Coating
Cost of Material*	\$ 36	\$ 68
Cost of Print	\$ 59	\$ Free
Surface Resistivity	10^7 to $10^9 \Omega$	10^6 to $10^9 \Omega$
Reliability	Resistance intrinsic to material higher likelihood of consistency	Potential of poor coating, inadequate curing
Lead time	1 week	1 week for print, 1 month for spray
Ease of printing	Higher temperature precision required to maintain resistivity	Simple to print

*Based on ESD-safe PLA and standard PLA.

A comparison between the two options is shown in Table 1. Although more expensive and a more technical print, the ESD-safe material is the preferred option because the surface resistance is intrinsic to the material. This increases the probability that the final printed material will have a consistent surface resistivity ranging between 10^6 and $10^9 \Omega$ versus the applied coating whose success is dependent on the coating and curing process, both of which are prone to error.

Even though most standard 3D printable filaments are available in an ESD-safe version, only two were considered due to general familiarity in print shops: ABS and PLA. When considering a 3D printing filament, there are a few main characteristics to examine: tensile strength, the maximum stress a material can withstand; Young's modulus, a measurement of stiffness in a material; tensile elongation, the amount a material can stretch from its original length before failing; glass transition temperature (T_g), temperature at which a filament begins to soften; and bed temperature, the required printing temperature to properly print a part. For this specific design, the material surface resistivity is also taken into account. Table 2 presents a comparison between the two considered filaments.

Table 2: Comparison specifications between ESD PLA and ESD ABS, both manufactured by 3DXTECH.

	3DXSTAT ESD PLA	Stratasys ABS-ESD 7
Tensile Strength	55 MPa	35.4 MPa
Young's Modulus	2560 MPa	2690 MPa
Tensile Elongation, Break	10 %	3.4 %
Glass Transition Temperature	60 °C	105.46 °C
Surface Resistivity	10^7 to $10^9 \Omega$	10^4 to $10^9 \Omega$
Bed Temperature	23 °C	110 °C

While the 3DXSTAT ESD PLA (PLA) is slightly more ductile and stronger than Stratasys ABS-ESD 7 (ABS), the ABS has greater stiffness than the PLA. However, the main distinguishing characteristics between these two materials are their temperature

dependence and surface resistivity. ABS has a much greater T_g than the PLA, meaning the ABS can survive in warmer conditions than the PLA, which increases the amount of continuous time the device can survive in warmer testing environments. Printing the ABS is more difficult than printing the PLA because the required bed temperature is much greater, and this ends up increasing printing cost. Then there is the difference in surface resistivity between the two filaments. The surface resistivity of the PLA is more restrictive than that of the ABS. The ABS surface resistivity range dips into the conductive region, which could affect the onboard electronics if the print job is substandard.

3.2.3 Final Design

The final housing is modeled in SolidWorks taking all design parameters into consideration. Fig. 18 illustrates the final housing model, which consists of a base that holds the evaluation circuit and a cover that seals the electronics from external exposure. The design is based on the dimensions and features of the evaluation circuit components.

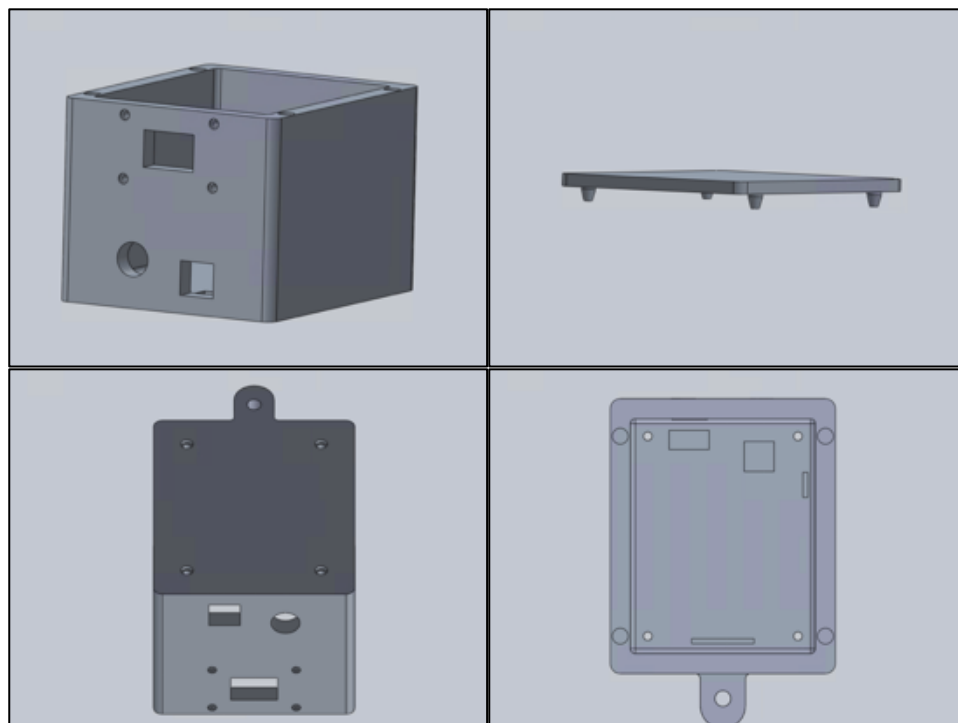


Fig. 18: 3D model: front view (top left), cover (top right), bottom front view (bottom left), aerial view (bottom right).

The usable area on the internal bottom face in the base is 70 mm × 90 mm, which is equivalent to the size of the evaluation board. The evaluation board includes four ESD-protected 3.2 mm diameter holes located 5 mm from their respective edges of the evaluation board. The holes are used to secure the board in a fixture. To utilize these in the housing, the bottom face of the housing is constructed with four positionally matched holes that include an offset on the external bottom face, Fig. 18 (bottom left), which allows for an M3 pan-head screw to slide through the hole and sit flush with the external face. Additionally, slits are included onto the bottom face of the housing to ensure the evaluation board sits flush inside the housing. Fig. 19 presents the main features that are accounted for. Within the internal faces, the slits are cut out at exact locations and designed larger than required to ensure no interference occurs even in the case of warping. The drawing for the bottom face is shown in Appendix A.3 and Appendix A.5.

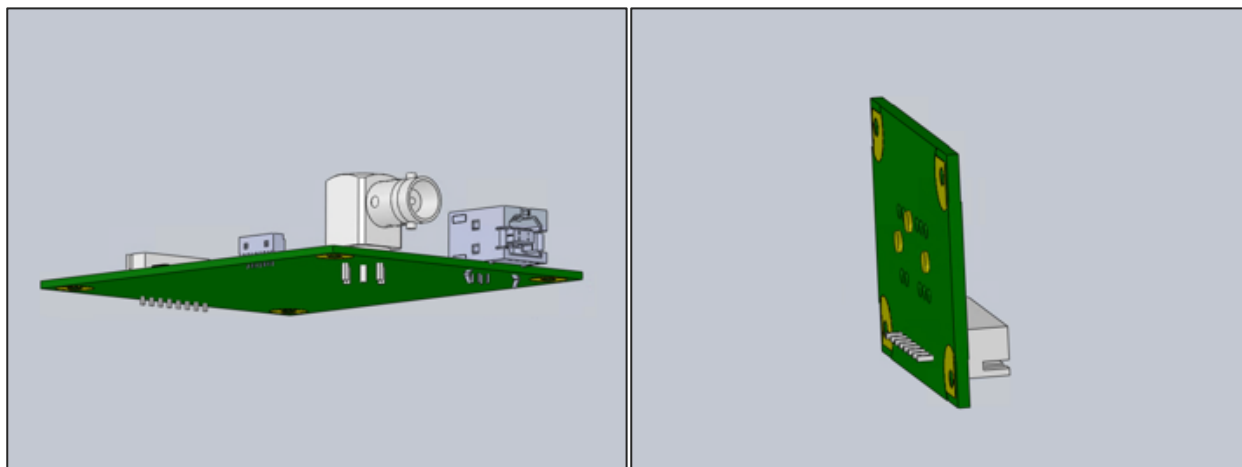


Fig. 19: SOLIDWORKS models of the evaluation board and sensor board.

The front face is designed to accommodate the sensor board and micro-spectrometer. The micro-spectrometer is centered on the sensor board. In the housing, the sensor board and micro-spectrometer are horizontally centered to the front surface with the width of the front face. The positional height of the sensor board and micro-

spectrometer center locations are chosen based on the flexibility of the connection cable. Large constant stress on the connection cable may eventually degrade the quality of signal transmission. Therefore, a height which allows for rigidity, but low stress, is optimal. A functional height for the sensor board and micro-spectrometer center is determined to be 54 mm above the evaluation board through manual testing.

The locations and sizes of holes and slits on the front face of the housing are positioned based on the determined center location and the dimensions of the sensor board and micro-spectrometer. The hole for the spectrometer is 21 mm × 14 mm, which provides enough space to allow for expansion and compression of material, as the micro-spectrometer is 20.1 mm × 12.5 mm. The sensor board is 29.6 mm × 43.6 mm, with ESD protected 2.2 mm diameter holes located 3 mm inwards from each respective edge. Similar to the bottom surface, holes are cut on the front face of the housing at respective sensor board hole locations with an offset on the external face to accommodate an M2 pan-head screw. Holes are also made on the front face of the housing for the USB 2.0 and BNC connection points. Additionally, a slit is constructed on the internal side of the front face below the micro-spectrometer hole such that the sensor board sits flush with the internal front surface of the housing and the micro-spectrometer stays optically aligned. The drawing for the front face is shown in Appendix A.1 and Appendix A.5.

The final housing design uses a 90 mm × 132 mm × 76 mm base and a 90 mm × 110 mm × 5 mm cover (Fig. 20). The base consists of 8 mm thick side walls and a 6 mm thick bottom base plate. The design also includes an attached ¼-20 inch screw slot for simple test setups on optical benches or with tripods.



Fig. 20: Final printed housing with cover.

The material for the housing is the 3DXSTAT ESD PLA, which is chosen based on its durability, surface resistivity and cost. The lead time and cost for each considered material are shown in Table 3.

Table 3: Lead time and cost comparison between two material options.

	3DXSTAT ESD PLA	Stratasys ABS-ESD 7
Lead Time	1 week	< 1 week
Cost	\$ 99	\$ 318

Although temperature resistance is an important parameter, most testing takes place in a laboratory environment, which limits the amount of high-temperature exposure. The minimal usage in a high-temperature environment does not justify the price point for ABS. Additionally, the ABS has a less restrictive surface resistivity range than the PLA.

Fig. 21 shows the evaluation circuit installed in the housing. The sensor board and micro-spectrometer are held into place using four plastic M2 pan-head screws and analogous M2 nuts. The evaluation board is secured to the housing using four M3 pan-head screws and M3 nut pairs. It is important to make note of a few subtle features within the final design that promote increased performance, functionality, and durability. First and foremost, all 90° edges are filleted to reduce the risk of warping and ghosting during the printing process. The cover pegs are chamfered at an angle of 75°, which minimizes the likelihood of a peg breaking off and a peg not fitting into the base due to thermal expansion (Fig. 19). Lastly, the ¼-20 inch slot extension is designed to fit a standard ¼-20 inch washer in case extra force is required to secure the housing down. Overall, the housing design effectively satisfies all design conditions and provides an effective and robust prototyping solution for the micro-spectrometer.

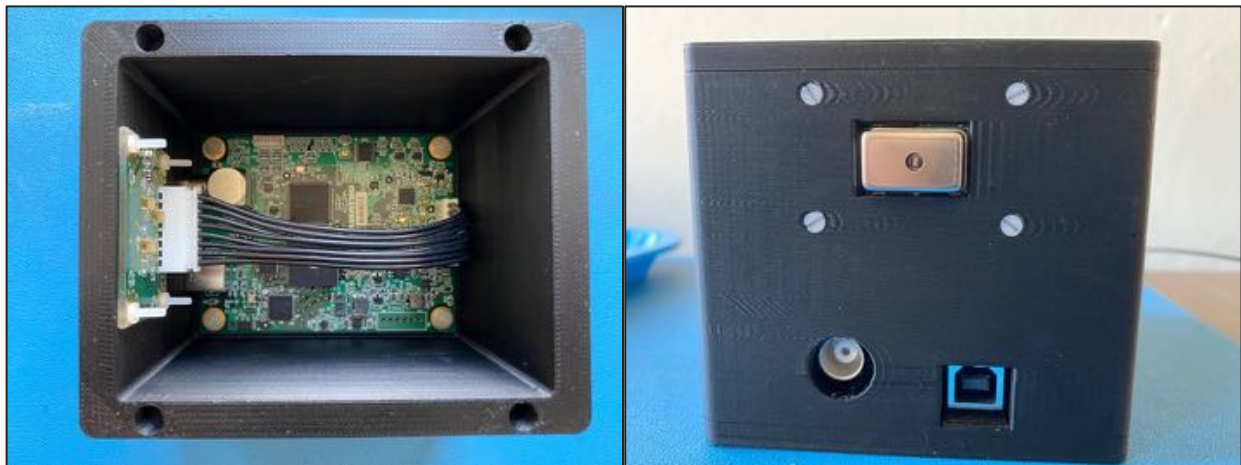


Fig. 21: Housing with integrated evaluation circuit.

Chapter 4: Characterization

The characterization of the C12880MA consists of measurements for detector linearity, FOV, optimal integration times, SNR, dark noise, temperature dependence, stray light, spectral resolution, repeatability, and surface reflectance retrieval. This section provides a discussion on the characterization testing objectives, setups, and parameters. Additionally, this chapter presents the radiometric calibration for the micro-spectrometer, which is performed in similar fashion to those of the GVRs and SpAM. The micro-spectrometer is characterized and calibrated in RSG laboratory facilities.

A 1 m diameter spherical integrating source (SIS) with a 25.4 cm circular aperture and ten 150 W bulbs is used for most of the laboratory characterizations. The bulbs of the SIS can be operated independently and illumination configurations of 1 to 10 bulbs are available for use. The SIS is a stable source and has been used by RSG since the 1990s.

4.1 Testing

4.1.1 Linearity

Detector linearity testing provides a characterization for how the micro-spectrometer responds to linear changes in input radiance levels and integration times. The laboratory linearity evaluations are performed using the SIS. For characterizing the detector linearity of the micro-spectrometer as a function of input radiance, a calibrated laboratory ASD spectroradiometer is used as a reference instrument to measure the radiance output of the SIS. The ASD and micro-spectrometer are placed side by side in front of the SIS to view the same target area (Fig. 22). Measurements are made simultaneously with both instruments at SIS configurations of 1, 2, 4, 6, 8, and 10 bulb

illuminations. The micro-spectrometer is set with an $11 \mu\text{s}$ integration time as none of the SIS configurations saturate the detector using this integration time.



Fig. 22: ASD spectroradiometer and micro-spectrometer set up in front of the SIS to view same target area for radiometric calibration.

Measurements for characterizing detector linearity as function of integration time are made using a similar setup. However, in this case the radiance output of the SIS is not measured with the ASD because the SIS illumination is held constant at 2 bulbs. Micro-spectrometer measurements are made at $11 \mu\text{s}$, $25 \mu\text{s}$, $50 \mu\text{s}$, $75 \mu\text{s}$, and $100 \mu\text{s}$.

An additional detector linearity evaluation is performed outdoors using a reference Spectralon panel and a 48 % reflective panel (Fig. 23). The panels are oriented towards the sun to maintain consistency with their laboratory calibration configuration. The integration time is held constant between the two measurements and is established by the highest integration time used to measure the Spectralon panel before saturation occurs. Measurements are made between 19:00 and 20:00 UTC on a clear and sunny day.



Fig. 23: Setup for making measurements with panels. The setup shown here is for measuring the Spectralon panel. The same setup is used to measure the 48 % panel.

4.1.2 Field of View

Characterization of the instrument FOV is necessary for system design and deployment. A characterization of the FOV establishes the spatial sample the instrument measures. Meanwhile, the deployment design takes the FOV characterization into consideration to ensure that the instrument does not see itself or shadows throughout the day.

The micro-spectrometer FOV is characterized using a simple test bed which includes a tripod, a Spectralon reference panel, and a black board. The reference panel is centered on a large surrounding area of black board. The micro-spectrometer is set with an 11 μ s integration time and the output signal is observed using the GUI's monitor mode (Fig. 15). The micro-spectrometer is traversed from the black board to the white Spectralon panel at a constant height above the panels until the first signal appears on the graph in the GUI (Fig. 24). At this position, the distance between the micro-spectrometer slit and panel, in the plane which the panel resides in, is recorded. Using

this distance and the height between the micro-spectrometer and panel, the FOV is calculated. The horizontal and vertical FOVs are measured using this test setup.



Fig. 24: FOV test setup. Spectrometer is traversed from the edge of the black panel to Spectralon panel in both x direction and y direction. Note: panel resting on spectrometer provides shade to the plastic and electronics during downtime and is not present during testing.

4.1.3 Optimal Integration Time for Field Use

Determining an optimal integration time for field use is a long-term characterization process. RRV surface illumination varies throughout the year due to changes in sun angle and weather conditions. The simplest deployment software setup would include a single programmed integration time that is capable of taking usable measurements for all “good” days. A “good” day for the RadCalNet occurs when the aerosol optical depth at 550 nm (AOD550) is less than 0.16, and the average BRF of the GVRs at each wavelength is within ± 1 standard deviation of the 2014-2019 GVR BRF average. The integration time used in field deployment should neither saturate the detector nor measure near dark levels for any measurements during these types of days.



Fig. 25: Setup for optimal integration time characterization. Measurements are made of the Spectralon panel and RRV soil. The instrument is positioned such that only the surface of interest is within the FOV.

The characterization process for the optimal integration time consists of taking measurements of RRV soil that RSG keeps at the University of Arizona. Measurements are taken at different parts of the year and are mostly made at solar noon (solar azimuth angle $\approx 180^\circ$). The characterization also includes taking measurements of the Spectralon panel concurrently with the RRV soil to determine minimum integration times. The longest integration time that does not saturate the detector when measuring the Spectralon panel provides a baseline integration time for measurements. The test setup has the micro-spectrometer in nadir viewing configuration over the RRV soil and the panel at a height that overfills the FOV with the surface of interest (Fig. 25).

4.1.4 Signal to Noise Ratio

A SNR characterization of the micro-spectrometer establishes the reliability of the instrument's data and determines if the instrument is a viable option for field deployment. For field deployment, the SNR of the spectrometer must be greater than the surface reflectance uncertainty specification of RadCaTS. The SNR for the micro-spectrometer is a spectral quantity and is the ratio of the signal, which is the dark corrected average over 100 consecutive scans, and the standard deviation of the 100 consecutive scans (Eq. 5).

$$SNR_{\lambda} = \frac{\text{Average signal of all scans}}{\sigma_{scans}}$$

Eq. 5

SNR measurements are made with the SIS. The light level of the SIS and integration time of the C12880MA are configured to keep the micro-spectrometer just below saturation. The setup is shown in Fig. 26. Additionally, SNR measurements are also made with the Spectralon panel, using a similar setup shown in Fig. 23.

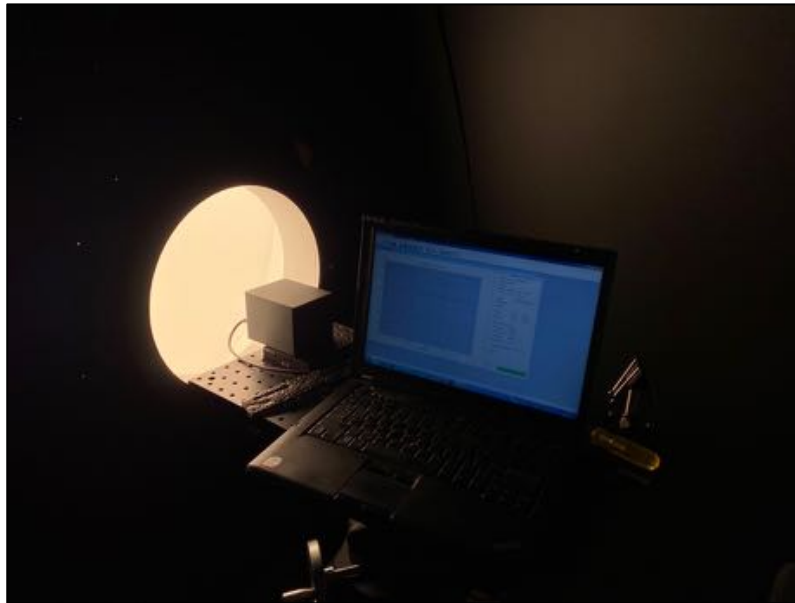


Fig. 26: Test setup for SNR measurements. The micro-spectrometer is centered with the output aperture of the SIS.

4.1.5 Dark Noise Characterization

Dark noise is a component of the system's overall inherent noise and arises mainly from the electrical noise within the system. The dark SNR of the micro-spectrometer should stay relatively constant over time and across all integration times. A characterization of the dark SNR determines if the spectrometer is operating in the same manner during each start up and maintains a consistent electrical noise factor. Dark measurements are taken by covering the entrance slit of the micro-spectrometer. For this characterization, measurements are taken at 11 μs , 50 μs , and 100 μs , using the dark

mode and measure mode in the GUI over a period of approximately 36 hours. Measurements are made using the two modes to determine if any differences other than file allocation exist.

4.1.6 Temperature Effects

The extreme conditions of RRV make it necessary to characterize the responsivity of the micro-spectrometer as a function of temperature. The temperature at RRV typically ranges between $-20\text{ }^{\circ}\text{C}$ and $45\text{ }^{\circ}\text{C}$ throughout the year. A characterization of the instrument's responsivity versus temperature determines if some form of temperature correction will be required for field deployment.

The SIS is used as the light source and as the heat source for this process. The SIS is illuminated with 8 bulbs and temperature readings are taken using a Minco 3 lead resistance temperature detector (RTD). The RTD is placed in direct contact with the sensor board using Kapton tape. The setup is shown in Fig. 27.



Fig. 27: Testing setup for measuring the responsivity dependence on temperature.

Measurements are made at temperatures between $13\text{ }^{\circ}\text{C}$ and $35\text{ }^{\circ}\text{C}$. In order to take measurements below ambient temperature, the micro-spectrometer is placed in a freezer until the RTD reads $-10\text{ }^{\circ}\text{C}$. Once the micro-spectrometer reaches this temperature it is

removed from the freezer and allowed to warm up to operation temperature in its test position, shown in Fig. 27. The integration time of the C12880MA is set to 25 μ s throughout the entire testing period.

4.1.7 Stray Light

The characterization of stray light provides data on how the micro-spectrometer is affected by out of field response. To be a field deployable instrument, the micro-spectrometer must attenuate stray light effects on its own or with an external housing design. Large amounts of stray light will degrade the quality of data as signal from out of view reflections and shadows will infringe on the signal coming from within the FOV. Stray light characterization determines if the device needs further customization, or if the current design is suitable for field deployment.

The stray light evaluation is performed using a lollipop test with the SIS. The lollipop test typically used by RSG consists of placing a black coated circle, the lollipop, directly in front of the instrument's aperture. The lollipop is centered within the SIS aperture and the instrument's aperture axis is aligned with the lollipop. The instrument is typically positioned such that the distance between the edge of the lollipop and the edge of the FOV of the instrument is less than 2.5 mm. The output of a perfectly designed instrument in this configuration would be zero [16].

The typical RSG lollipop test setup is slightly modified for the stray light characterization of the C12880MA. Rather than positioning the micro-spectrometer where the edge of FOV and edge of lollipop are separated by less than 2.5 mm, the micro-spectrometer is placed on a translation stage 9.5 mm from the lollipop and translated away from the lollipop an additional 58 mm (Fig. 28).

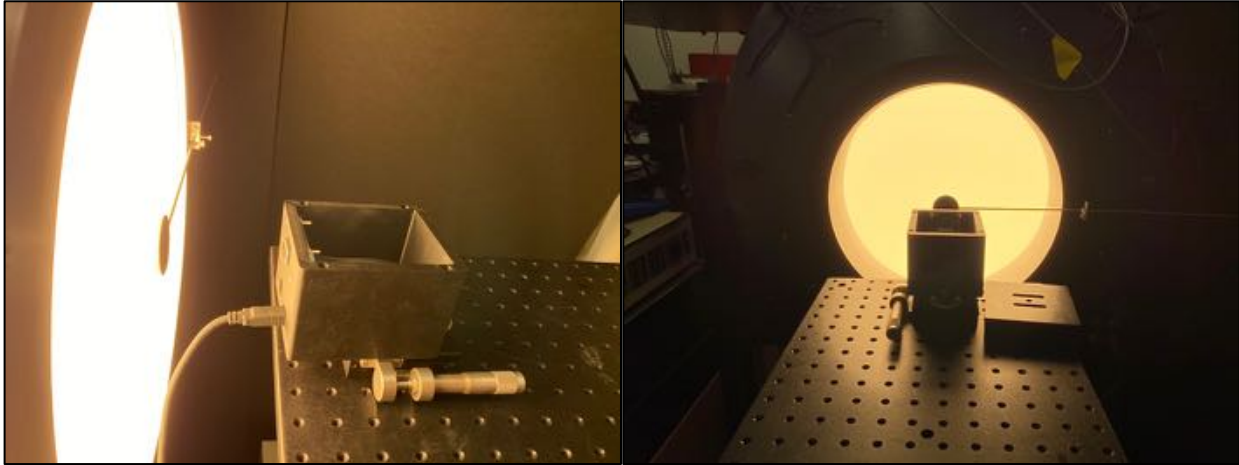


Fig. 28: Lollipop test setup for the micro-spectrometer.

The point at which the edge of the FOV of the micro-spectrometer and the edge of the lollipop is 2.5 mm occurs 38 mm away from the lollipop. The sphere is illuminated with 6 bulbs. Measurements are taken periodically using a 50 μ s integration time. The micro-spectrometer is characterized in its bare aperture state. The percent stray light seen by the micro-spectrometer is calculated using Eq. 6.

$$\% \text{ Stray light} = \frac{\text{Signal with lollipop}}{\text{Signal without lollipop}} * 100$$

Eq. 6

4.1.8 Spectral Characterization

The spectral characterization includes multiple instrument characterizations, the first of which is the spectral resolution. The spectral resolution is defined as the FWHM of a wavelength. Secondly, the spectral characterization shows if there is any out of band detection in the instrument. Lastly, the spectral characterization verifies the accuracy of the given spectral calibration.

A 0.6 mW 543 nm laser and a 0.6 mW 633 nm laser along with the SIS are used for the spectral characterization. The micro-spectrometer is placed directly in front of the SIS, and the laser is placed behind the micro-spectrometer and aligned such that the

initial beam spot is located away from the micro-spectrometer's target area in the SIS (Fig. 29). The SIS is illuminated by the laser. Measurements are made using integration times of 11 ms, 50 ms, and 100 ms.



Fig. 29: Laboratory setup for spectral characterization. Left picture is a top view of the setup, spectrometer is centered in the sphere aperture and the laser is positioned to send an unobstructed beam into the SIS. Right picture shows the green laser illuminating sphere. The red laser is substituted for the green laser during the 633 nm measurement.

4.1.9 Repeatability

A characterization of repeatability determines the instrument's consistency and stability over time. The repeatability of the micro-spectrometer is characterized by comparing independent measurements of the SIS. An independent measurement is one where the instrument is set up for operation, measurements are made, the instrument is turned off, and the setup is disassembled. For this characterization, independent measurements that are taken a month and a half apart are used for comparison. A calibrated laboratory ASD is used to measure the radiance output of the SIS and is a reference instrument for this characterization.

4.1.10 Surface Reflectance Retrieval

Surface reflectance retrieval is the process of analyzing the surface reflectance profile measured by the micro-spectrometer for characteristics found in the surface's

known reflectance profile. The output of the micro-spectrometer should follow the typical spectral shape of the surface under test. This characterization provides verification that the micro-spectrometer is properly dispersing the input light.

For the characterization, grass and asphalt are used as target surfaces. Since the quantity of interest for this characterization is surface reflectance, the process of taking measurements roughly emulates the surface measurement process used in the reflectance-based approach. The integration time for all measurements is set using the maximum allowable time when measuring the Spectralon panel. The dark-corrected signal measurements are converted to surface reflectance through Eq. 1. The setup for measuring asphalt is shown in Fig. 30, and it is the same setup used for the other surface reflectance measurements. For a panel measurement, the panel is oriented towards the sun and the micro-spectrometer is positioned in a nadir viewing configuration so that panel overfills the micro-spectrometer FOV. For a surface measurement, the micro-spectrometer is positioned in a nadir viewing configuration so that the surface of interest overfills the FOV. These measurements are made during clear and sunny conditions to minimize effects due to changes in the solar illumination.



Fig. 30: The setup for measuring the surface reflectance of asphalt. The same setup is used for other surface measurements.

4.2 Radiometric Calibration

The last phase of the characterization process for the micro-spectrometer is the absolute radiometric calibration. The radiometric calibration determines the radiometric calibration coefficient, C , for each micro-spectrometer wavelength. The calibration coefficient has units of $\frac{W*s}{DN*m^2*um*sr}$, and it converts the time-independent output signal (DN) of each pixel to a radiance value using Eq. 7, where DN_{signal} is the dark corrected signal.

$$L = C * \frac{DN_{signal}}{Integration\ Time}$$

Eq. 7

The objective of the preliminary radiometric calibration is to analyze how consistently and accurately the micro-spectrometer outputs spectral radiance using a singular radiometric calibration in different environments. The radiometric calibration is performed using a calibrated laboratory ASD spectroradiometer as a transfer radiometer, and the SIS. The micro-spectrometer and ASD are placed in front of the SIS aperture and the two instruments are positioned to roughly share the same target area in the SIS (Fig. 22). Measurements with the ASD spectroradiometer and the C12880MA are taken simultaneously. Three total radiometric calibrations are performed, one for each integration time: 11 μ s, 50 μ s, and 100 μ s. The SIS is illuminated using 6 bulbs, 4 bulbs, and 2 bulbs, respectively.

Once measurements are made, post processing of the micro-spectrometer data is required to calculate the calibration coefficients. The ASD outputs resampled radiance at a 1 nm interval, while the micro-spectrometer spectral calibration gives wavelength values to the third decimal value. The wavelengths for the micro-spectrometer that are nearest

to a whole integer value, a difference less than 0.1, are chosen for the direct calculation of a calibration coefficient. The dark-corrected signals for these wavelengths are divided by the specific integration time used during testing to remove the time dependency on the signal. The ASD-measured radiance at the correlating wavelengths is then divided by the time-independent dark-corrected signals, yielding the calibration coefficients. Using MATLAB, a linear fit is applied to the directly computed calibration coefficients for all wavelengths in the micro-spectrometer spectrum to obtain a calibration coefficient at each wavelength.

Chapter 5: Results

The next step in completing the characterization of the micro-spectrometer is processing the raw data. This chapter presents the processed results for each characterization test, including a description of the data processing procedures. The results are summarized for each characterization.

5.1 Characterization Results

5.1.1 Linearity

The detector linearity evaluation for various radiance levels is shown in Fig. 31 and Table 4. Fig. 31 shows the dark-corrected signal versus the relative radiance measured from the SIS by the ASD for specific wavelengths.

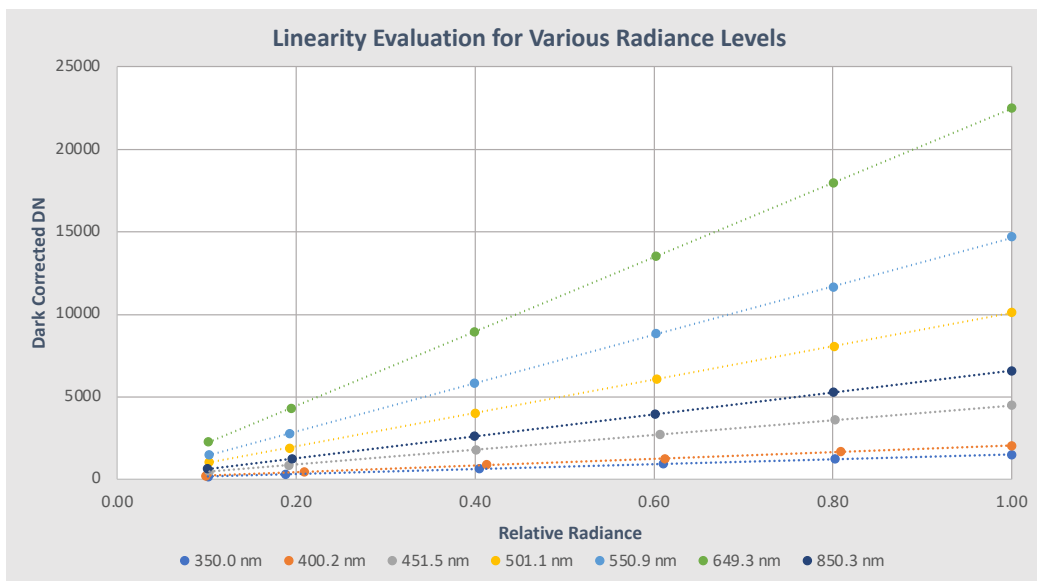


Fig. 31: Linearity evaluation for different radiance levels. The dark corrected signals for each wavelength are plotted versus the relative radiance.

The relative radiance is the ratio of the radiance from the respective bulb configuration to the radiance at the 10 bulb configuration, and it is unitless. A linear fit is performed on the dark-corrected DN data, and it is used to calculate the linearity error (Table 4). Generally, the error is less than 2 % at each radiance level for each wavelength, but there are three

outliers: the 350.0 nm and 400.2 nm channel at the 1 bulb configuration, and the 400.2 nm at the 2 bulb configuration.

Table 4: Linearity percent error from linear fit of the micro-spectrometer for different radiance levels.

		Number of Bulbs on in SIS					
		1	2	4	6	8	10
Wavelength (nm)	350.0	6.8	0.5	0.5	1.1	2.4	2.0
	400.2	15.6	5.0	1.8	0.1	1.9	1.6
	451.5	2.0	0.8	0.0	0.1	0.2	0.2
	501.1	1.4	0.6	0.0	0.0	0.4	0.2
	550.9	1.6	0.5	0.1	0.1	0.4	0.2
	649.3	0.9	0.3	0.0	0.0	0.3	0.2
	850.3	0.1	0.6	0.0	0.1	0.4	0.2

The measurements for the detector linearity as a function of integration time are analyzed in similar fashion as the linearity evaluation for various radiance levels. The data are dark corrected and graphed versus their respective integration times per specific wavelength. The linearity plot is shown in Fig. 32 along with the linear fit. The linearity error is shown in Table 5. The linearity error for the different integration times at each wavelength is generally less than 1 %.

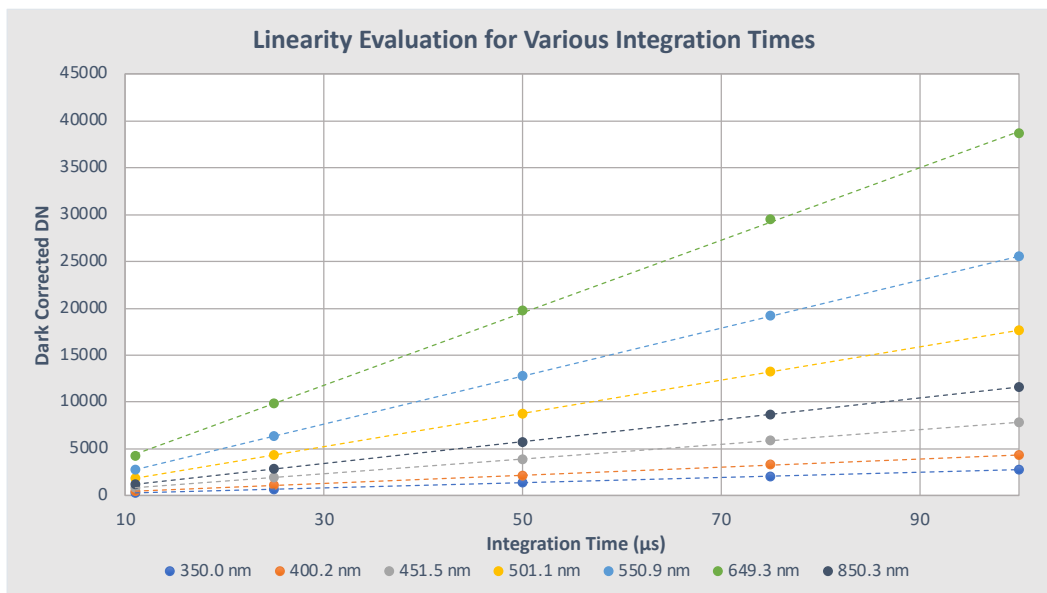


Fig. 32: Linearity evaluation for various integration times. The dark corrected signals for each wavelength are plotted versus the integration time used during measurement.

Table 5: Linearity percent error from linear fit of the micro-spectrometer for different integration times.

		Wavelength (nm)						
		350.0	400.2	451.5	501.1	550.9	649.3	850.3
Integration Time (μ s)	11	0.6	0.9	1.2	0.8	0.0	3.2	0.8
	25	0.2	0.2	0.5	0.0	0.0	0.5	0.1
	50	0.3	0.1	0.1	0.3	0.1	1.0	0.3
	75	0.0	0.4	0.0	0.0	0.2	0.8	0.1
	100	0.1	0.2	0.0	0.1	0.1	0.7	0.0

For the detector linearity evaluation performed using the 48 % panel and Spectralon panel, the dark-corrected signals measured from the 48 % panel and Spectralon panel are compared against each other. In addition, the ratio between the measurement of the 48 % panel and measurement of the Spectralon panel is compared to the ratio between the laboratory measured BRF of the 48 % panel and Spectralon panel. The top graph in Fig. 33 shows the dark-corrected signal of each panel measurement. The bottom graph displays the two ratios and the percent error between the ratio of the DN data and the ratio of the laboratory BRF. In a perfectly linear system these two ratios should be equal. The percent error is calculated using

$$\% \text{ error} = \left| \frac{\text{Experimental} - \text{Theoretical}}{\text{Theoretical}} \right| * 100$$

Eq. 8

where the experimental value is the ratio from DN measurements, and the theoretical value is the ratio of the laboratory BRF. One source of error in the linearity evaluation may originate from the panel not being oriented exactly with the solar azimuth angle. Further, another error may arise from discrepancy between the source angle for which the BRF values are interpolated and the solar zenith angle at the time of measurement. Data are only considered from 400 nm to 845 nm for the bottom graph, as these wavelengths

define the overlap between the calibration of the panels and the micro-spectrometer's wavelengths

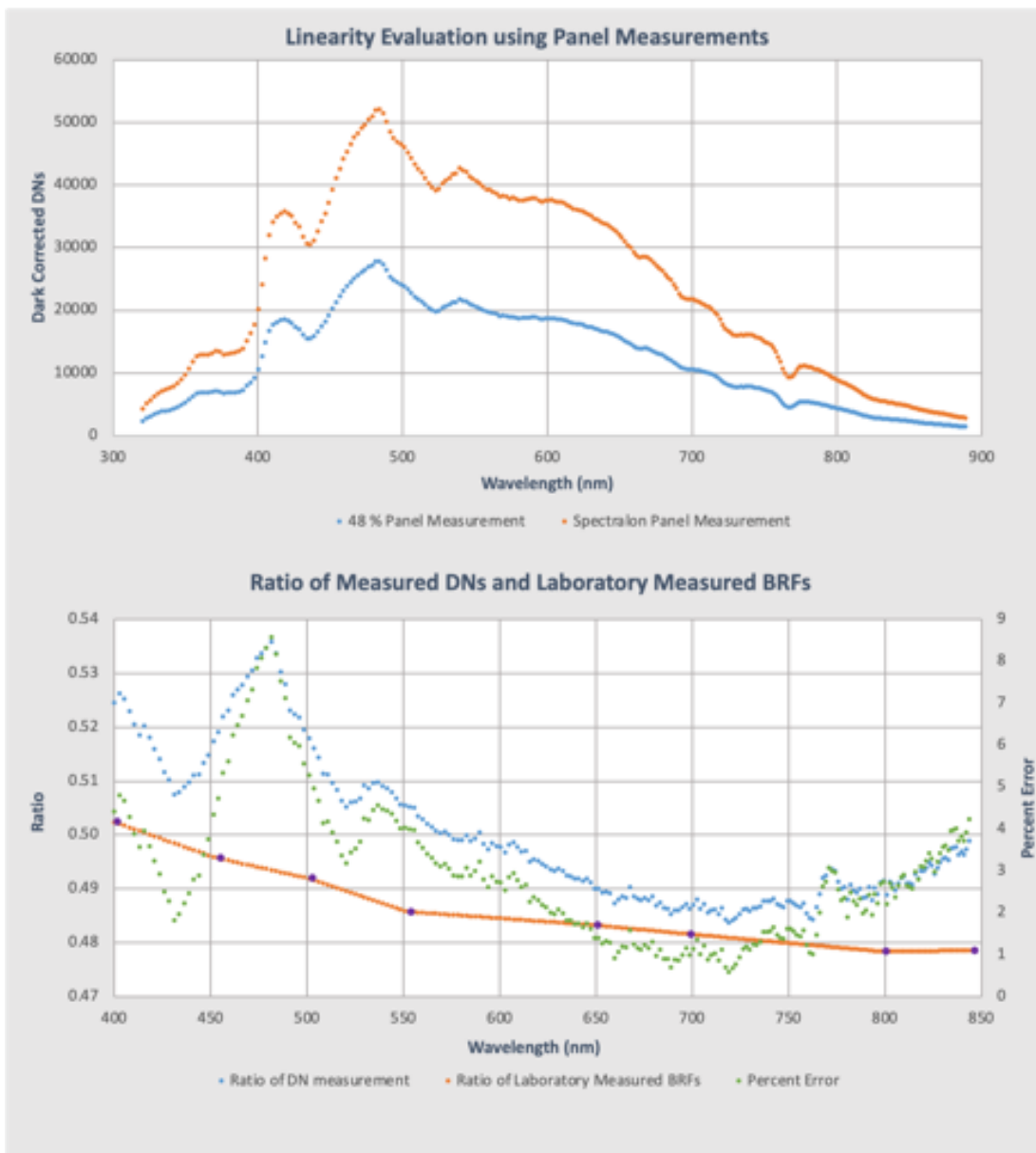


Fig. 33: Linearity evaluation using Spectralon panel and 48 % reflective panel. Top graph shows the dark corrected DNs of the two panels measured with the micro-spectrometer. Bottom graph shows the ratio of the measured DNs, and the ratio between the laboratory measured BRFs for the panels. The measurements are taken at a SZA of 45°.

Purple marker points are the wavelengths for which calibration measurements are taken at, orange is the interpolation of these values onto the micro-spectrometer's spectrum.

5.1.2 Field of View

The horizontal FFOV of the micro-spectrometer is determined to be approximately 34° and the vertical FFOV is approximately 44°. For the horizontal FFOV measurement,

the first signal appears on the GUI when the micro-spectrometer is 23.5 cm above the panel and 7.6 cm to the side of the panel. For the vertical FFOV measurement, the first signal appears on the GUI when the micro-spectrometer is 23.5 cm above the panel and 11.4 cm to the side of the panel.

5.1.3 Optimal Integration Time for Field Use

Measurements to determine the optimal integration time for field use were made between October 2021 and February 2022 at UArizona. Tucson and RRV are both situated in semi-arid locales with clear skies throughout much of the year, but it is important to note that the difference in altitude (~750 m for Tucson vs. 1435 m for RRV) means that the atmospheric transmission, and therefore the solar irradiance, will differ slightly in each location for a given solar zenith and azimuth illumination angle. The process of adjusting the integration time for instruments tested in Tucson and deployed to RRV is a typical adjustment made by RSG before deployment. The final integration time is typically determined using in situ measurements during the final deployment.

For measurements in Tucson during this period the optimal integration time is ~140 μ s. The micro-spectrometer output signal at this integration time is ~12000 DN's lower than saturation for measurements taken at solar noon. When one takes the surface reflectance and atmospheric transmission at RRV during the summer months into account, the optimal integration time for deployment can be estimated using the ratio between the cosine of the solar zenith angle measurements taken in Tucson to other dates at RRV. As mentioned, further adjustments to the final integration time will take place at RRV during the initial deployment of the micro-spectrometer(s).

5.1.4 Signal to Noise Ratio

The SNR measurements using the SIS are made using 6 bulbs with a 45 μs integration time and 4 bulbs with a 70 μs integration time. SNR measurements of the panel are made using a 50 μs integration time. The SNR for the micro-spectrometer is dependent on the wavelength and source (Fig. 34). The SNR profiles for the SIS measurements are quite similar to each other with peaks around approximately 650 nm, while the panel measurement peak occurs around 500 nm. The SNR ranges between a minimum of 50 and a maximum of approximately 300.

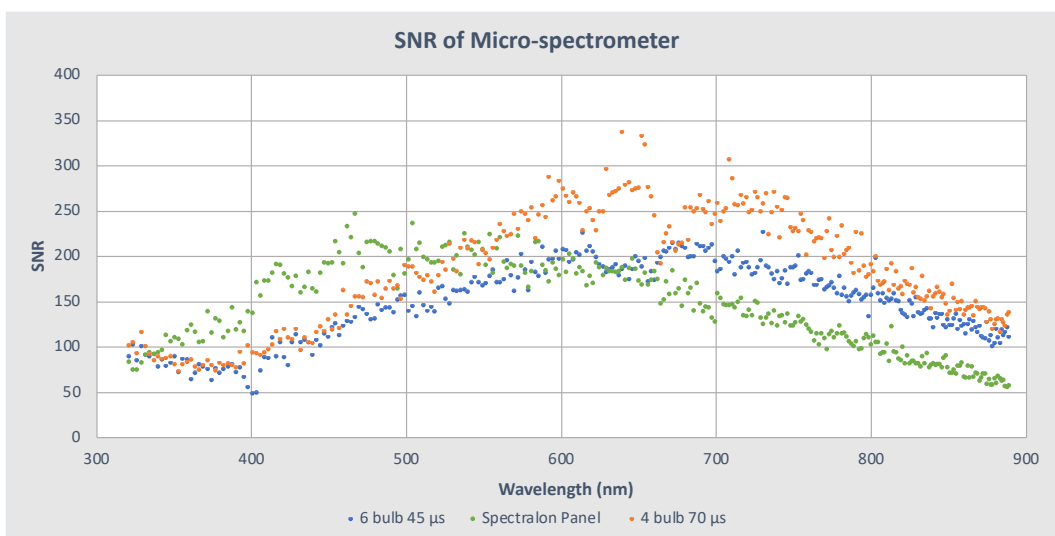


Fig. 34: SNR vs wavelength for 3 different sources.

Table 6 shows the SNR for specific wavelengths. Table 6 further emphasizes the variation in SNR for different sources.

Table 6: SNR values for specific wavelength channels from different sources.

		Wavelength (nm)						
		350.0	400.2	451.5	501.1	550.9	649.3	850.3
Source	6 bulb 45 μs	90	49	122	140	170	189	124
	4 bulb 70 μs	81	95	119	189	204	261	140
	Spectralon Panel	111	137	193	197	191	173	71

5.1.5 Dark Noise Characterization

The dark noise characterization is a measurement of the dark reading SNR. While Table 7 only shows the 550.9 nm channel, the data from this channel are representative for the dark SNR measurements over the entire micro-spectrometer spectrum.

Table 7: Dark reading SNR for 550.9 nm channel over a span of 36 hours and 29 minutes. Measurements shown are taken using dark mode in the system GUI.

		Integration Time (μ s)		
Duration (HH:MM)		11	50	100
	0:00	144	147	154
	20:41	158	169	170
	24:15	187	196	157
	36:29	150	173	166

The dark SNR values over the entire spectrum vary between 130 and 190, with minimal consistency or patterns. The lower range of dark SNR values are normally only seen for the measurement taken at start-up, 0:00, confirmed by data in Table 7. Although, there is randomness between individual wavelengths, the average dark SNR after warm-up, which considers measurements taken after 0:00, is 173 with a standard deviation of ± 13 . Additionally, large differences are not observed in the average dark SNR for measurements made using dark mode versus measure mode (Fig. 15).

5.1.6 Temperature Effects

The micro-spectrometer's responsivity dependency with temperature is characterized between 13 °C and 35 °C. Fig. 35 shows the temperature dependence of the system responsivity for specific wavelength channels. A linear fit is applied to the data. The linear fit in Fig. 35 indicates that there is a direct relationship between system responsivity and temperature.

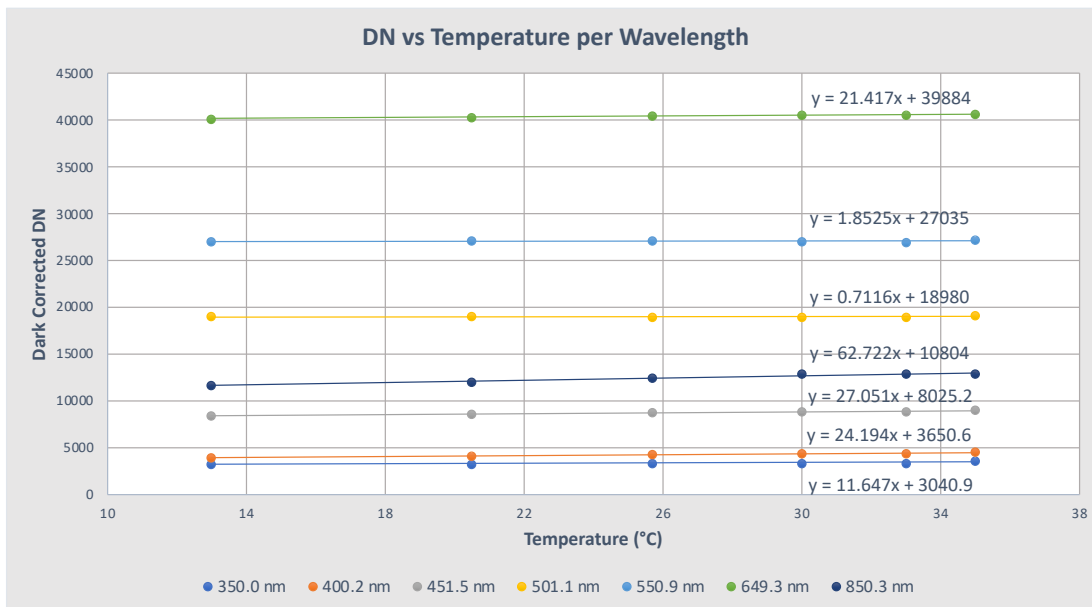


Fig. 35: Temperature dependence for the system responsivity for specific wavelengths. A linear fit is performed on the measurements.

Fig. 36 shows the percent difference between the ambient temperature measurement, 25.7 °C, and the other temperature measurements.

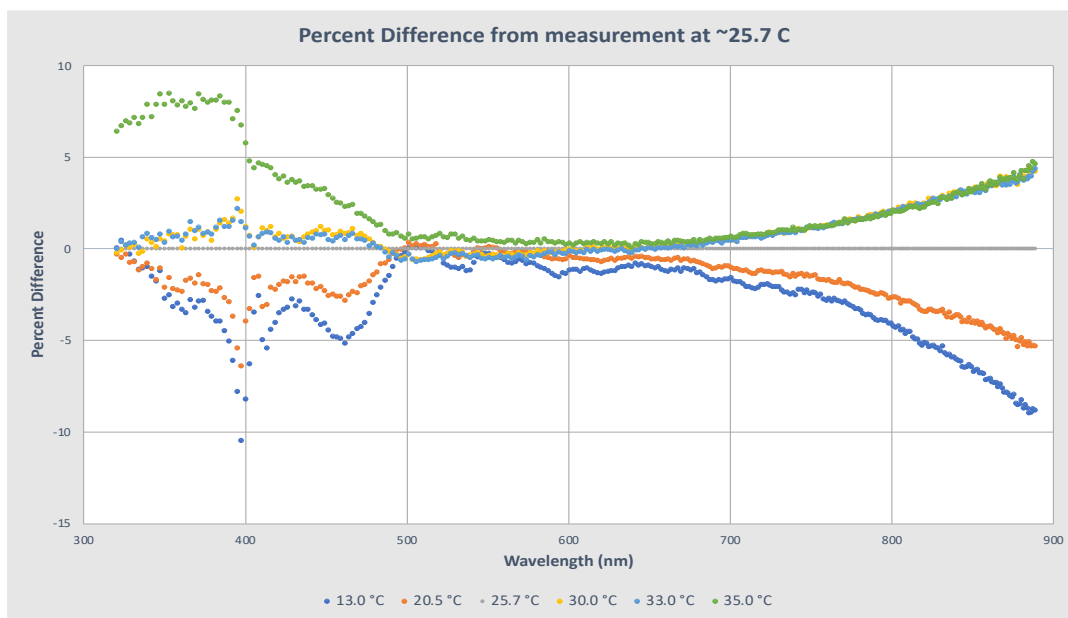


Fig. 36: Percent difference of measurement from the ambient measurement (25.7 °C).

The percent difference is calculated using Eq. 8, where the ambient measurement is considered the theoretical value and the other temperature measurements are considered the experimental values. The sign is included in this percent difference

calculation to better visualize how temperatures above and below the ambient temperature affect the system output. The ambient temperature is zeroed for this data.

5.1.7 Stray Light

The characterization of the stray light profile for the micro-spectrometer is shown in Fig. 37. The 9.5 mm measurement is zeroed for this data set. At this separation distance between the micro-spectrometer and lollipop, the micro-spectrometer's FOV is completely blacked out and only the ambient room light is entering the system. Thus, the 9.5 mm measurement is subtracted from every measurement including itself to remove any signals from ambient lighting. Eight total measurements are taken at the distances shown in the legend of Fig. 37. A separation of 2.5 mm between the micro-spectrometer's FOV and the edge of the lollipop occurs when the separation distance between the two objects is 38.1 mm.

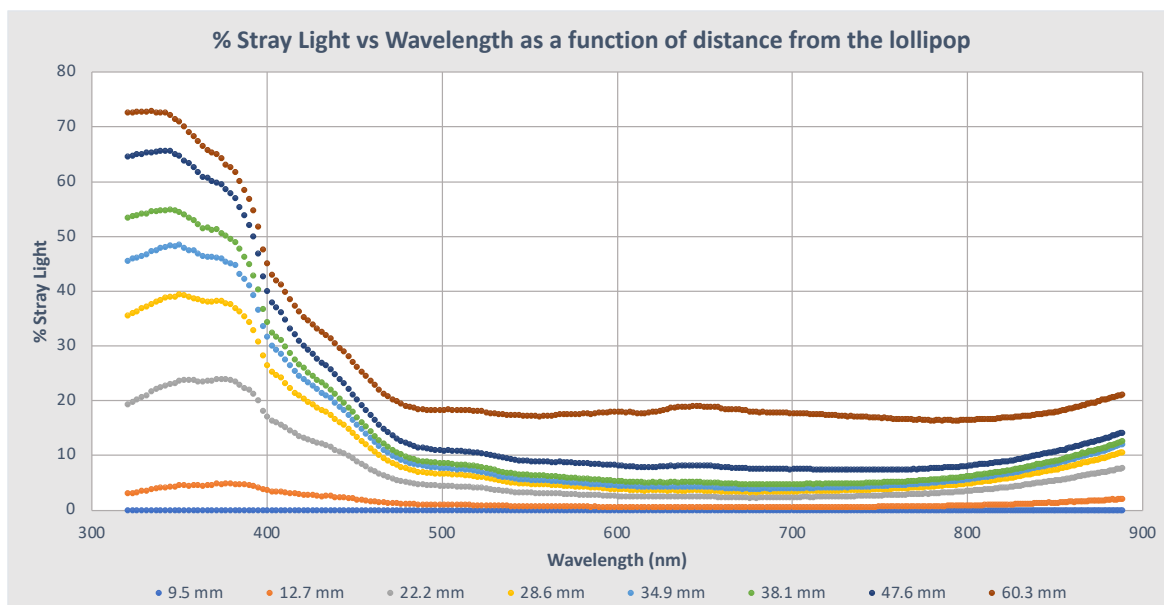


Fig. 37: Stray light characterization as a function of distance from the lollipop.

5.1.8 Spectral Characterization

The spectral characterization measurement is shown in Fig. 38 and Fig. 39. The raw data is dark corrected and normalized. The data in Fig. 38. represents the 100 ms

integration time measurement. Both green and red laser measurements are included in Fig. 38 along with their peak wavelength and approximate spectral resolution values. Fig. 39 shows the spectral characterization on a log scale for analysis of out of band detection.

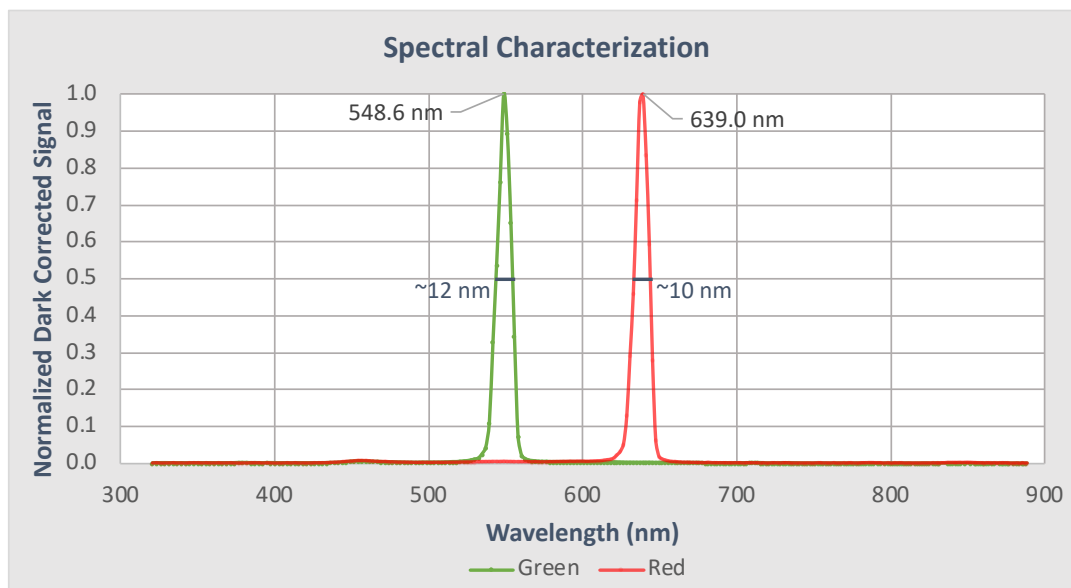


Fig. 38: Spectral characterization of the micro-spectrometer for a 543 nm and 633 nm lasers for a 100 ms.

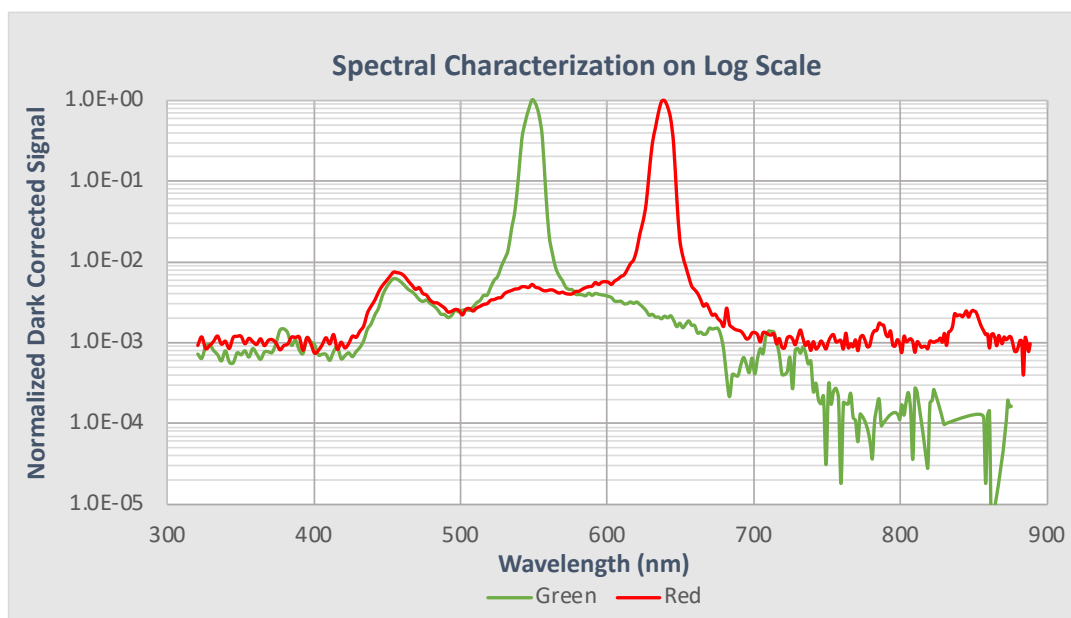


Fig. 39: Spectral characterization plotted on a log scale to observe the out of band response by the C12880MA

5.1.9 Repeatability

The micro-spectrometer's repeatability characterization is shown in Fig. 40. The measurements compared are of the SIS at 10 bulb illumination and the micro-spectrometer at an 11 μs integration time. The data compared is taken on 12 August 2021 and 30 September 2021. A radiometric calibration is created from the 12 August data and is applied to the 30 September data. Percent difference is calculated by comparing the micro-spectrometer radiance from 30 September 2021 to the corresponding radiance output from the SIS measured with the ASD. The percent difference is between 30 % and 3 % from 350 nm to 500 nm and stays below 5 % for the rest of the wavelength range.

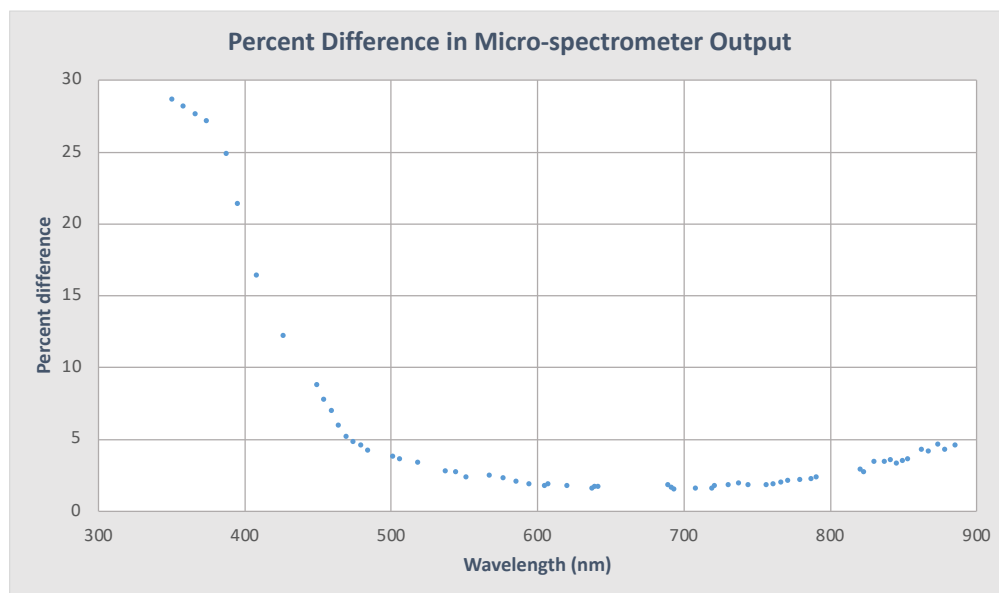


Fig. 40: Percent difference in micro-spectrometer output of data taken on 12 August 2021 and 30 September 2021.

5.1.10 Surface Reflectance Retrieval

Fig. 41 presents the surface reflectance retrieval measurements for asphalt and grass. For the measurements taken with the C12880MA, both asphalt and grass measurements are taken using the same integration time, 50 μs , on 03 February 2022. All measurements are taken at similar times during the day, approximately ± 30 minutes

from solar noon. In addition, the same reflectance measurement process is used for both surfaces.

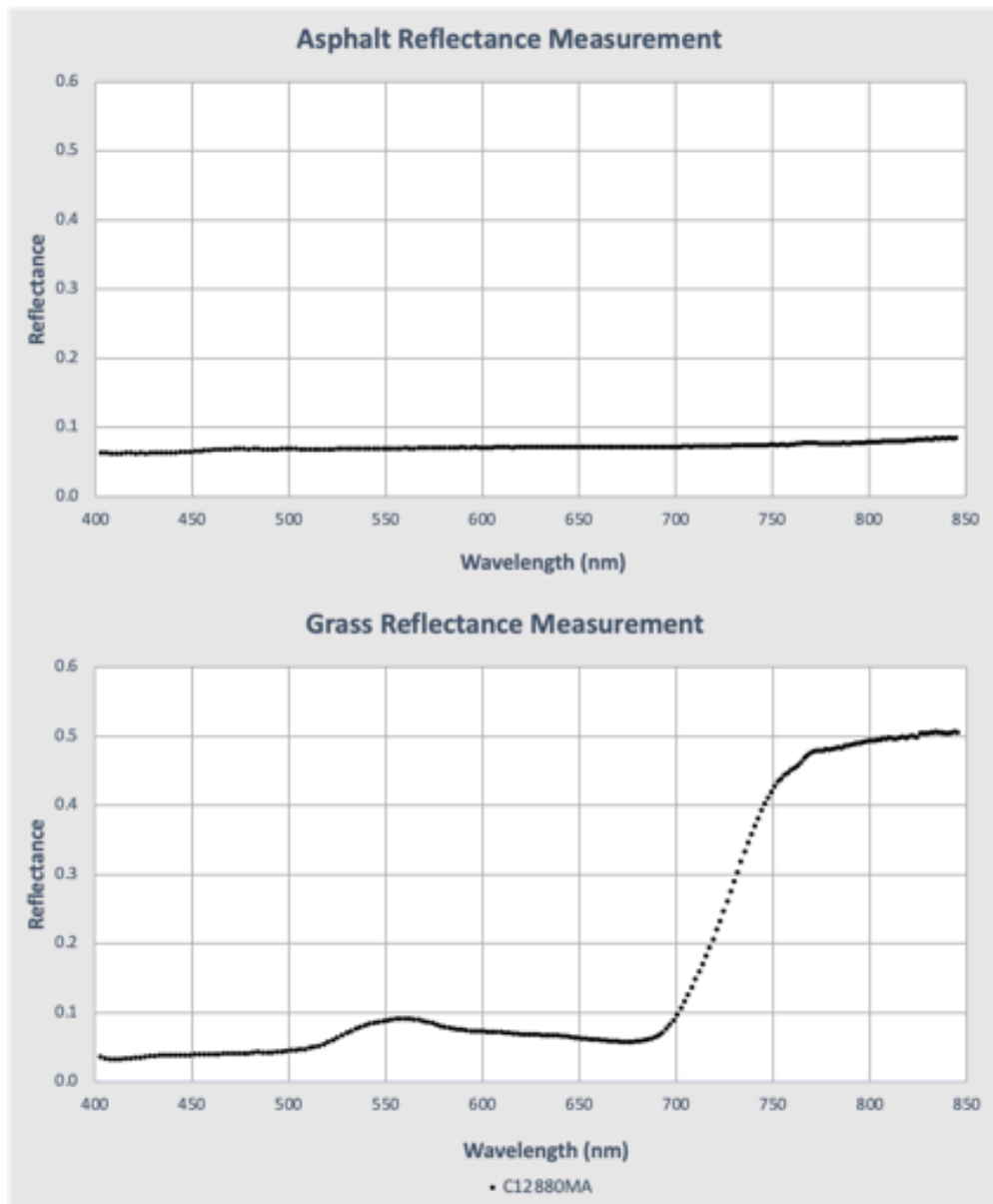


Fig. 41: Reflectance measurements for asphalt and grass surfaces. The black curves represent reflectance measurements taken with the C12880MA.

5.2 Radiometric Calibration Results

The radiometric calibration coefficients for each calibration are shown in Fig. 42. The calibration coefficients span a wavelength range of 350 nm to 885 nm. Wavelengths lower than 350 nm are excluded from the radiometric calibration because they are not

within the ASD's spectrum. The values of the calibration coefficients are directly related to the wavelength. The three calibration results are quite similar to each other until approximately 800 nm, after which there is a visible variation between the results.

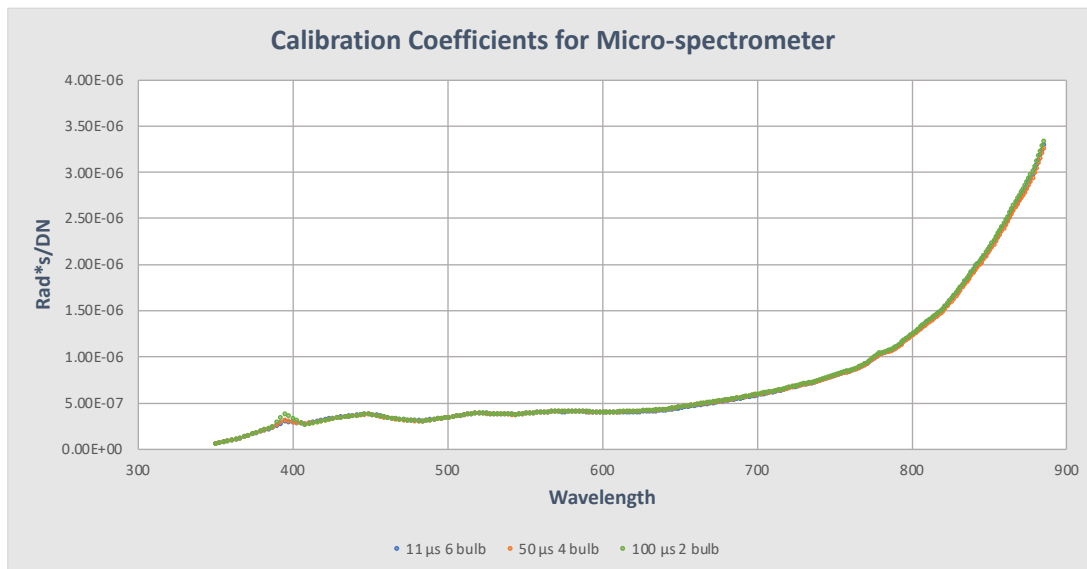


Fig. 42: Calibration coefficients for the micro-spectrometer for each radiometric calibration.

Chapter 6: Discussion and Future Work

6.1 Discussion of Laboratory Characterization

The characterization results show the C12880MA to be a suitable instrument that has a few limitations in its measurement capabilities and accuracy. Beginning with detector linearity, the C12280MA is generally linear for most wavelengths with input radiance and with integration times. Table 4 shows that the C12880MA is more linear for mid-level input radiances and wavelengths from 450 nm to 850 nm. While still below 3% from 350 nm to 450 nm, the linearity error is greater for this region than it is at longer wavelengths. A similar trend is observed in the linearity error with integration time, the higher wavelengths and longer integration time yield a lower error than shorter wavelengths and lower integration times.

The SNR as a function of wavelength meets and exceeds the RadCaTS SNR requirement for all wavelengths. Fig. 34 shows the C12280MA's wavelength dependence on SNR. The SNR is generally rising from 322 nm up to 500 nm (and 650 nm), depending on the source. It increases up to as much as 350. After its peak in that regime the SNR gradually tapers off up to the end of the wavelength range. The SNR relationship with wavelength is similar to that of the detector sensitivity versus wavelength relationship (Fig. 10) and the general SNR curve shape (Fig. 34) can be attributed to that relationship. The dark SNR on the other hand does not display a correlation with sensitivity and wavelength. The values vary with randomness wavelength to wavelength and integration time to integration time. The dark SNR, however, can be accurately characterized by, excluding the 0:00 measurement, its average and standard deviation values.

The C12880MA has a responsivity dependence on temperature as shown in Fig. 35 and Fig. 36. There is a direct relationship between the signal and temperature, which is supported by the consistency of positive slope values for each linear fit in Fig. 35. The percent difference from the ambient temperature signal (Fig. 36) shows that a much stronger temperature effect on responsivity exists from 322 nm to 500 nm, and 750 nm to 888 nm, than between 500 nm to 750 nm. A similar wavelength trend is observed in the stray light characterization. From 322 nm to ~500 nm, and 750 nm to 888 nm, the stray light detected by the instrument is much greater than the stray light detected between 500 nm and 750 nm. While the percent stray light increases after 750 nm, the percent stray light from 322 nm to 500 nm is overbearing in comparison. Based on the characterized FOV there should have been no stray light effects at or below a distance of 38.1 mm from the lollipop for the C12880MA, however as Fig. 37 shows, stray light effects exist and are prominent at that position and prior to it as well. Further testing is required to determine how much of a temperature correction will be required for deployment as well as to determine the optimal correction for stray light effects.

The spectral characterization verifies the spectral resolution that is provided by the manufacturer (Fig. 10). As for out of band detection, at approximately 450 nm there is a slight out of band signal detected, however, the detection is less than 1 % of the peak signal and should not affect field measurements. The results also show an inaccuracy in the absolute spectral calibration applied to the instrument by Hamamatsu. For the test, a 543 nm green laser and 633 nm red laser were used as light sources. The respective measured peaks occur at 548.6 nm and 639.0 nm, which is an error of 5.6 nm and 6.0

nm, respectively. Moreover, dark-corrected DNs of measurements taken outdoors show the oxygen absorption band at 767.0 nm rather than at ~760.0 nm.

The C12880MA shows a wavelength dependence in the repeatability characterization, similar to the one observed in the stray light and temperature dependence characterization. Between 350 nm and 475 nm, the error of the measured radiance from 30 September 2021 is much larger than in any other wavelength range. As the wavelength begins to approach the 800 nm and on region, the error again begins to increase. From 500 nm to 750 nm, however, the repeatability error is around 1.5 %, which is still large but not as drastic as the outer wavelength regions. The repeatability needs to be continuously monitored to ensure that the C12880MA consistently has similar or better results.

As for the surface reflectance retrieval, the general trends seen in known grass and asphalt reflectance profiles are observed in the C12880MA measured surface reflectance. The grass BRF measurement with the C12880MA displays the red edge at approximately 675 nm which is a specific characteristic of the grass BRF. Additionally, there is a spike at 550 nm representing the green profile of grass. Secondly, the measured asphalt BRF follows the typical non-spectral reflectance response of asphalt. The C12880MA BRF measurements accurately mirror the typical surface reflectance profiles of grass and asphalt.

The radiometric calibrations as shown in Fig. 42 begin to differentiate from each other starting at ~800 nm. This discrepancy is much more apparent when applying the calibration to raw data. Other than error at wavelengths greater than 800 nm, the radiometric calibrations are comparable to each other, specifically between 400 nm and

800 nm. In this wavelength region, there are minimal discrepancies between the coefficients. While the calibrations are comparable to each other, their output versus analogous ASD radiance data can be erroneous. In some cases, one calibration outperforms the others when comparing with corresponding ASD radiance data. Further testing is required to create a single and accurate radiometric calibration that is applicable to any measurement.

6.2 Summary of Thesis

The Hamamatsu C12880MA is a candidate for integration into RSG's RadCaTS suite of instruments. It is an ultra-compact grating based micro-spectrometer that operates from 322 nm to 888 nm. This thesis presents the initial development, which includes the prototyping and characterization, of the C12880MA for automated field deployment. The device is prototyped with a 3D-printed ESD-safe instrument specific housing and evaluation circuit, and it is characterized in RSG's laboratory facilities.

The results from this work establish the micro-spectrometer's characteristics, which provide insight into the measurement functionality and accuracy of the C12880MA. The data show that the C12880MA is an effective instrument in most aspects. Generally, it performs accurately between 450 nm and 800 nm, a similar wavelength range to SpAM. Measurements from 322 nm to 450 nm and after 800 nm are observed to have greater error and inconsistencies than those made from 450 nm to 800 nm. While the accuracy of the measurements across its entire spectrum is not as precise as other deployed instruments, the appeal of an efficient, reproducible, and easily-deployable instrument remains for the C12880MA. The results of this work show that, if optimized for measurements between 400 nm and 800 nm, the C12880MA can provide RSG with an

easily deployable, integrable, and reproducible instrument that can reduce the uncertainty in RadCaTS results.

6.3 Future Work

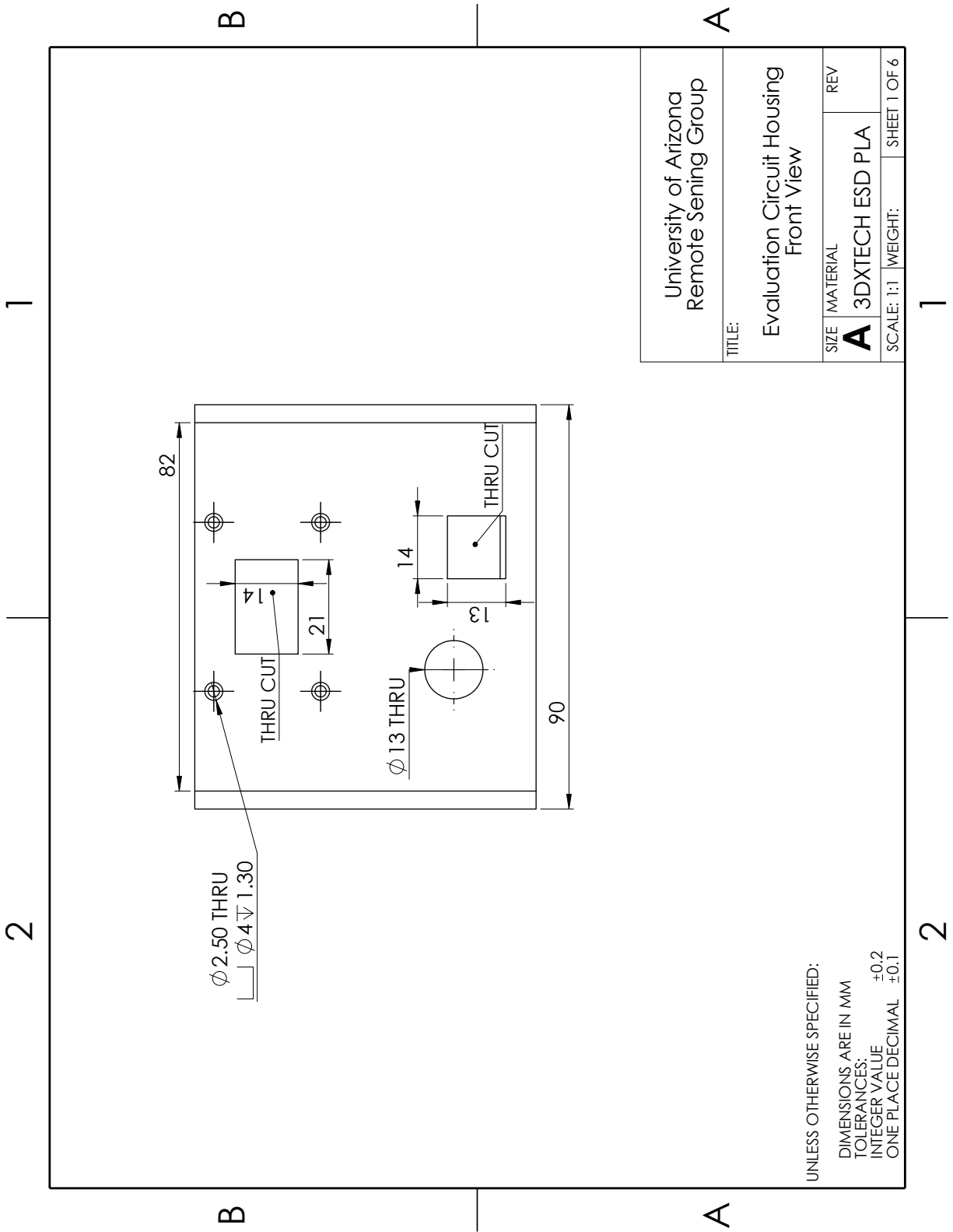
The next phase for the development of the C12880MA is to configure it for deployment and integration to RadCaTS. The system will need to eventually consider measurement corrections, software design, and mechanical assembly for deployment. In terms of measurement corrections, the C12880MA needs further testing and analysis to determine an optimal operating wavelength range. In addition, the spectral and radiometric calibrations need to be improved or be taken into consideration during post-processing for higher accuracy. Moreover, the stray light effects and temperature dependence on the radiometric responsivity will have to be mitigated in the final design. As for software, the future work will include creating a program that allows for autonomous operation. This can be approached through the manufacturer-provided development code, external Arduino kits, and external triggers. The final instrument software will need to be able to take measurements on an exact time interval and relay the measurements back to RSG via the satellite uplink base station in RRV. For the final system, the C12880MA needs to be housed in an ESD safe environment and be weather proofed to survive the extreme weather conditions of RRV. The C12880MA will also need its own power supply system for remote operation.

The long-term outlook for the development of the C12880MA is to eventually deploy and integrate many of these instruments to RadCaTS. Deploying multiple instruments will increase the total spatial sample measured of the surface and continue to reduce the uncertainty in RadCaTS results. Once one fully designed C12880MA is

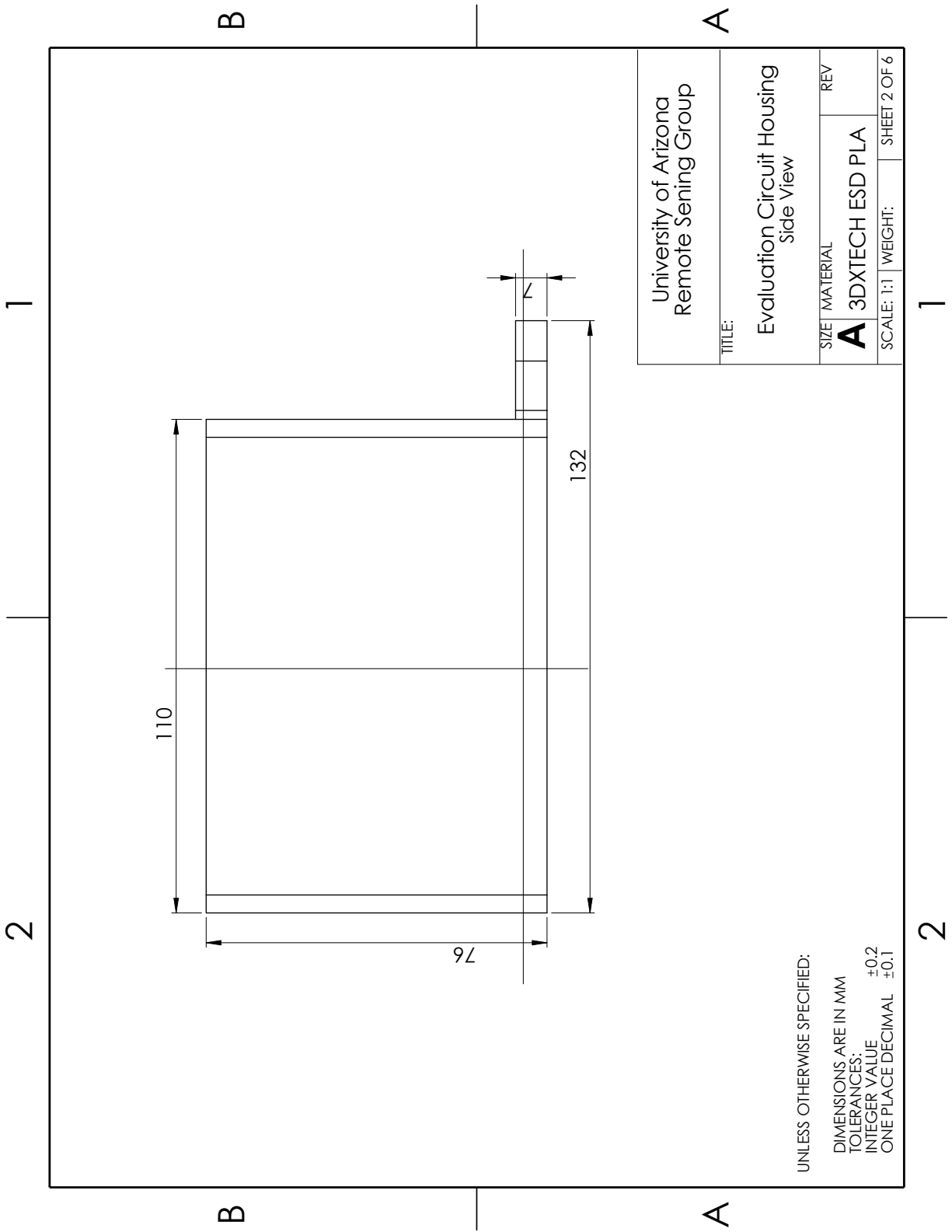
deployed and proven to be a functional and accurate field instrument, RSG should be able to mass produce the micro-spectrometers because of their compact size and simple design.

Appendix A: Housing Drawings

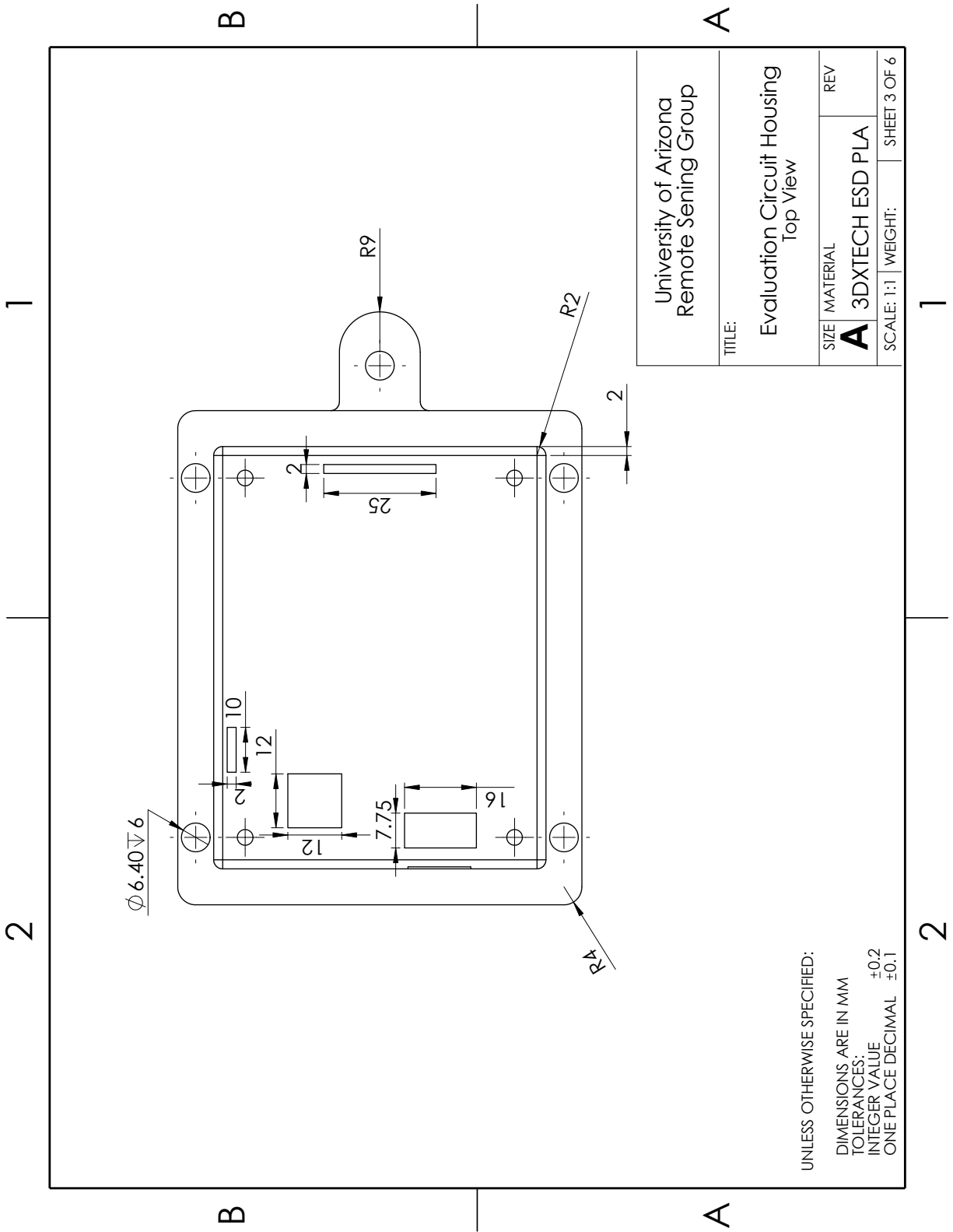
A.1 Front View of Housing



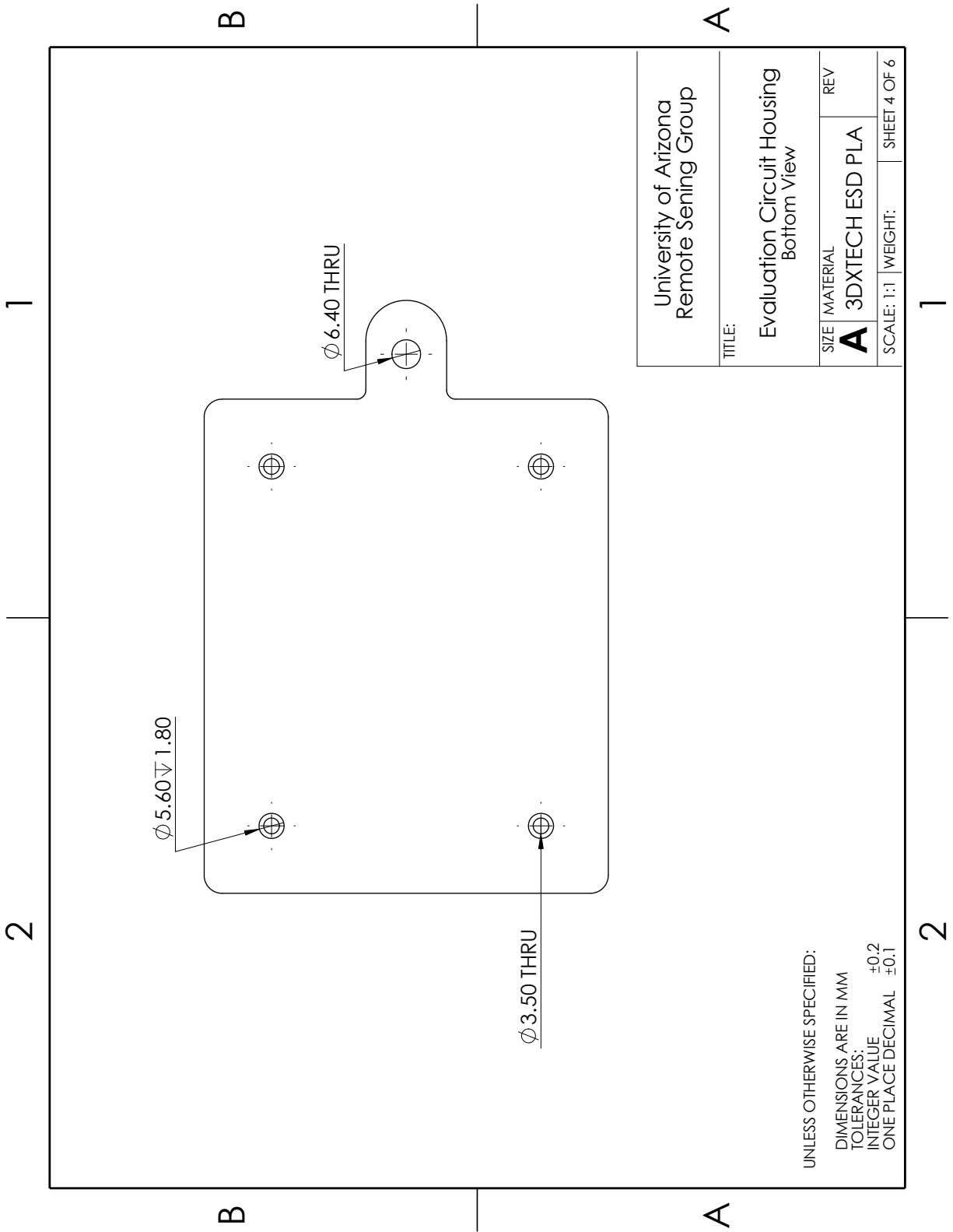
A.2 Side View of Housing



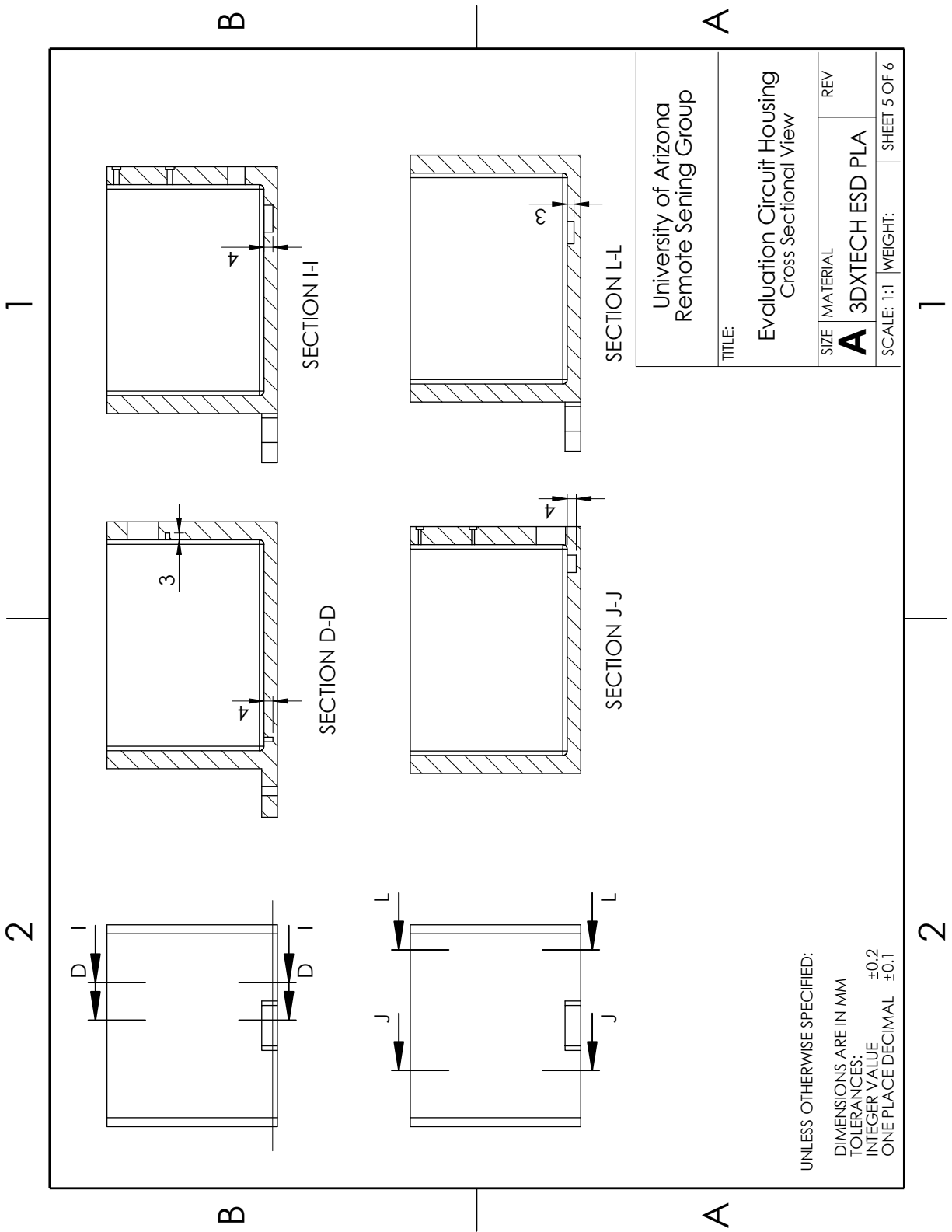
A.3 Top View of Housing



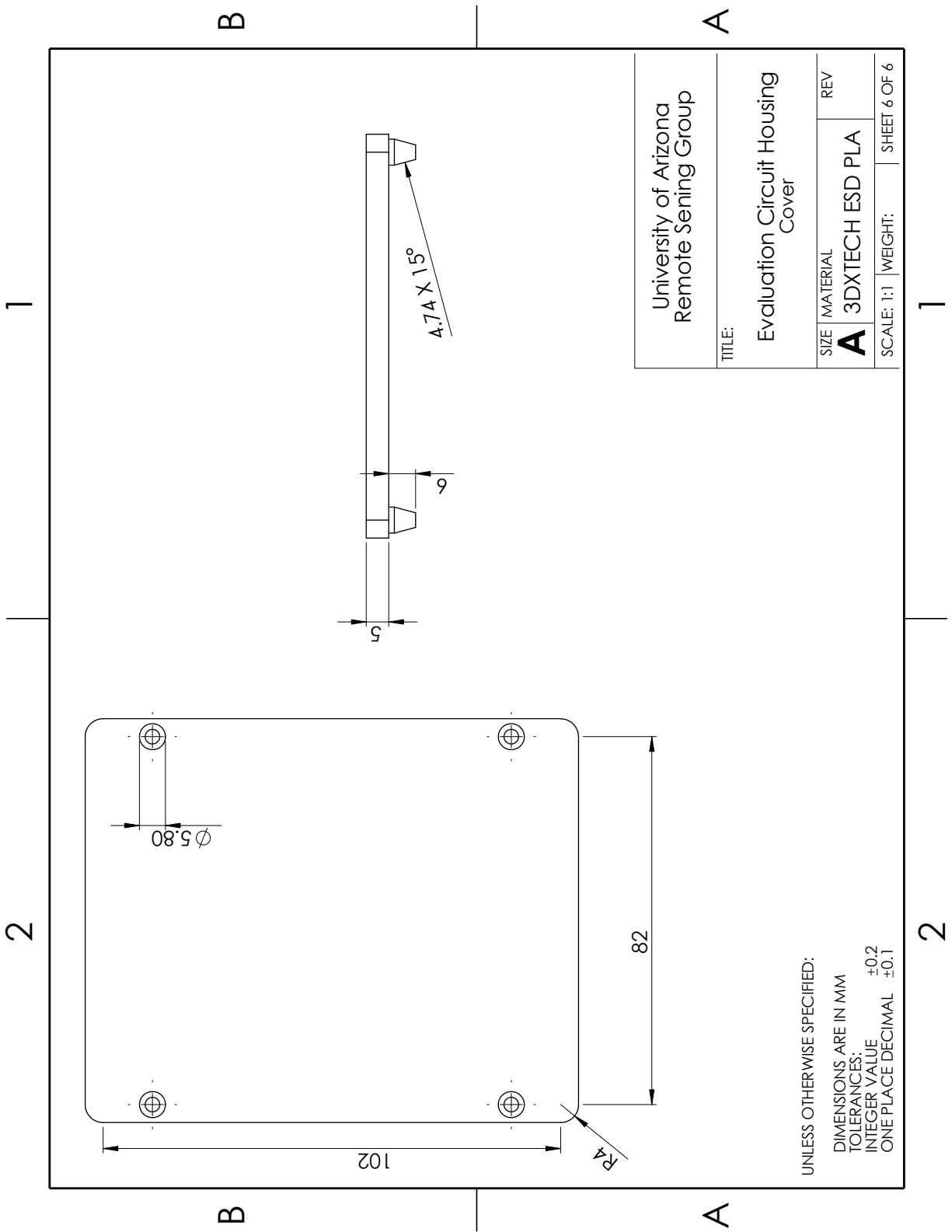
A.4 Bottom View of Housing



A.5 Cross Sectional View of Housing



A.6 Cover of Housing

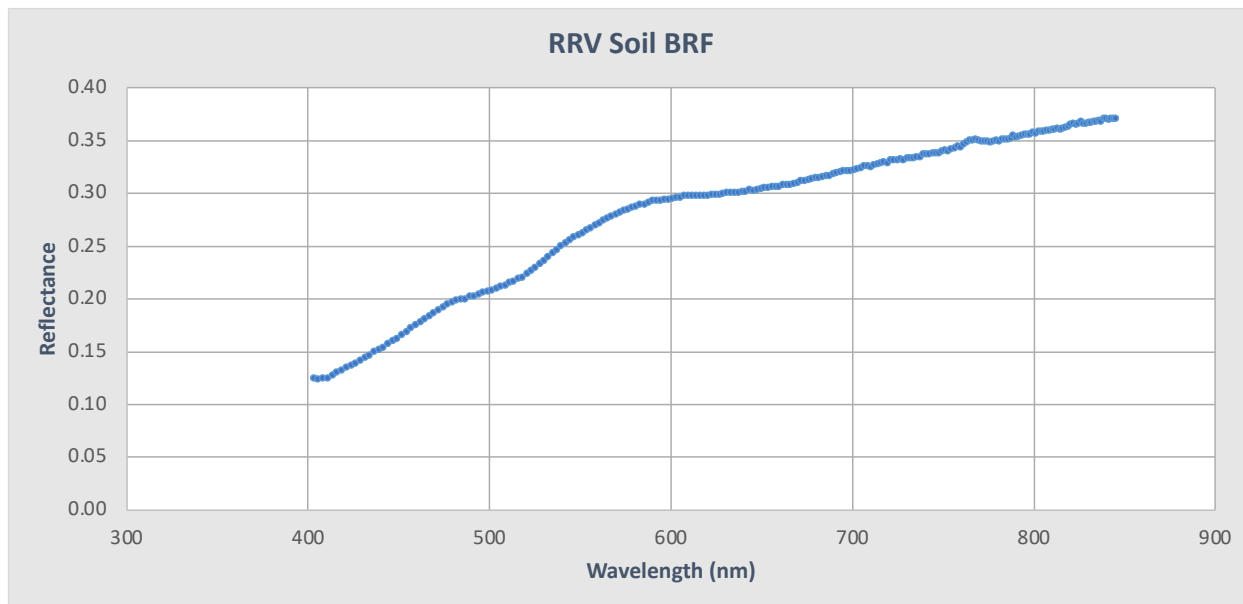


University of Arizona Remote Sensing Group	
TITLE: Evaluation Circuit Housing Cover	
SIZE	MATERIAL
A	3DXTECH ESD PLA
SCALE: 1:1	WEIGHT:
REV	
SHEET 6 OF 6	

UNLESS OTHERWISE SPECIFIED:
 DIMENSIONS ARE IN MM
 TOLERANCES:
 INTEGER VALUE ± 0.2
 ONE PLACE DECIMAL ± 0.1

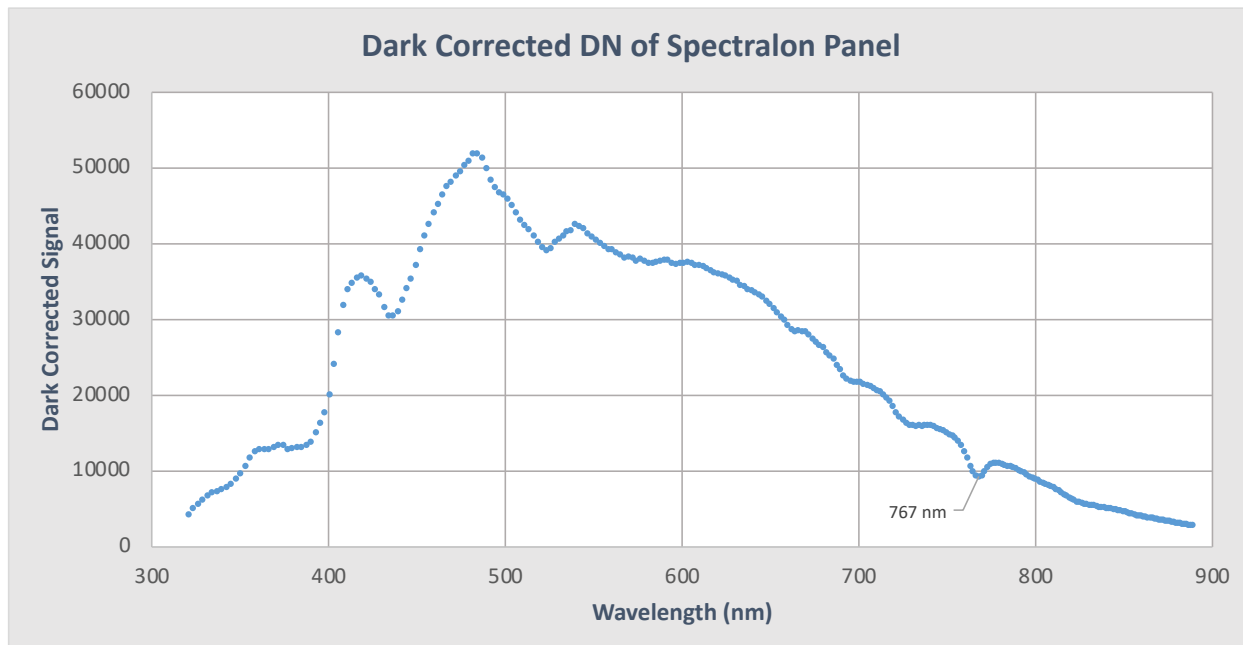
Appendix B: Additional Results

B.1 RRV Soil BRF



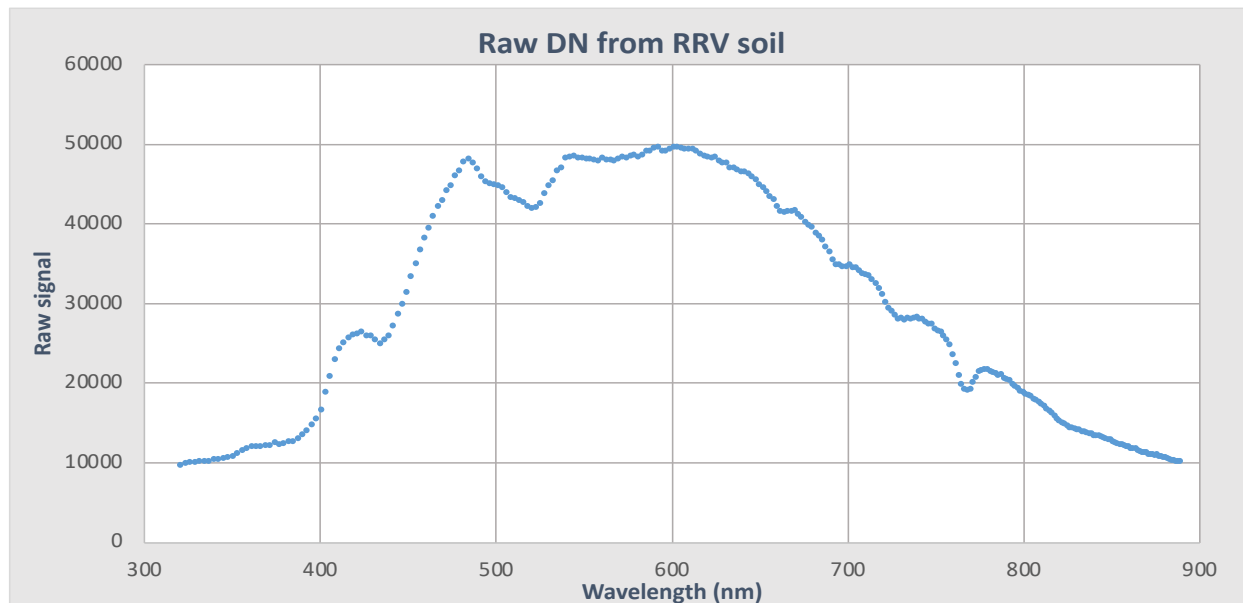
RRV BRF measurement taken at the University of Arizona on 22 February 2022 using a 40 μ s integration time

B.2 Signal from Spectralon Panel



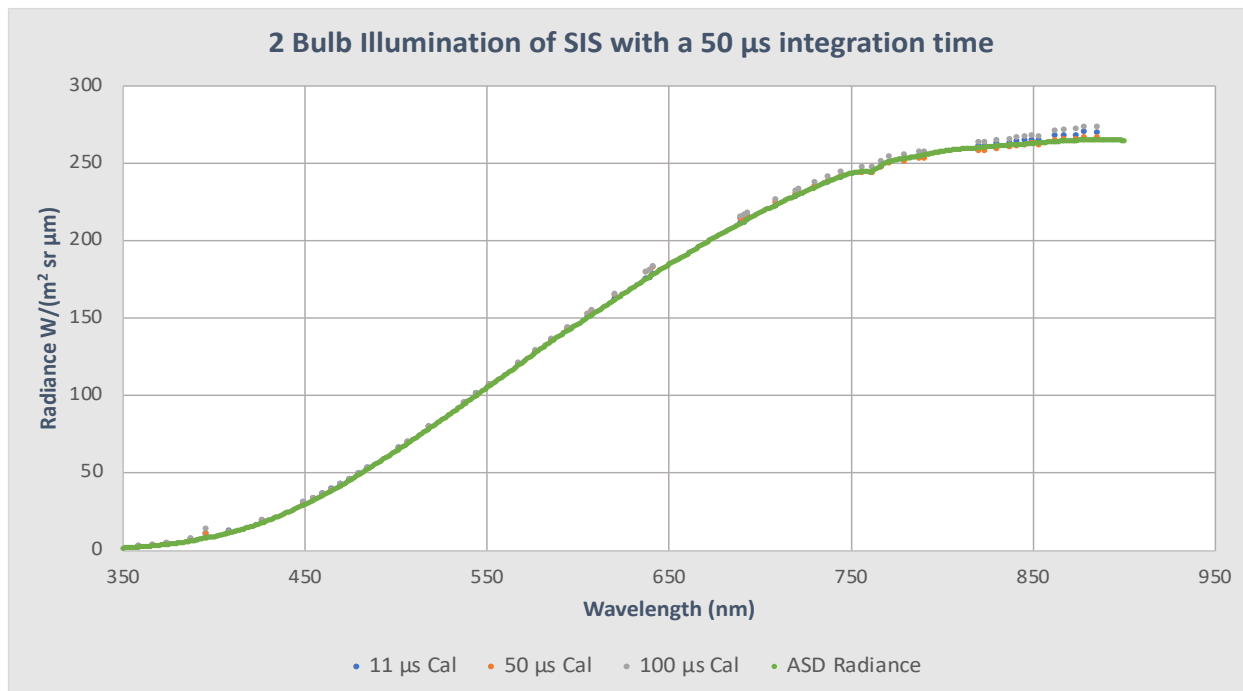
Dark corrected signal for measurement of Spectralon panel using a 40 μ s integration time showing the Oxygen band on 21 October 2021

B.3 Signal from RRV soil



Raw signal measured off RRV soil on 22 February 2022 using a $160 \mu\text{s}$ integration time

B.4 Radiometric Calibration Comparison



Radiance measured by the micro-spectrometer for the SIS with a 2 bulb illumination and a $50 \mu\text{s}$ integration time. Each radiometric calibration is applied and plotted against the ASD measured radiance

References

1. Slater, P.N., et al., *Reflectance- and radiance-based methods for the in-flight absolute calibration of multispectral sensors*. Remote Sensing of Environment, 1987. **22**(1): p. 11-37.
2. Anderson, N., et al., *Design and calibration of field deployable ground-viewing radiometers*. Appl. Opt., 2013. **52**(2): p. 231-240.
3. Czapla-Myers, J., et al., *The Ground-Based Absolute Radiometric Calibration of Landsat 8 OLI*. Remote Sensing, 2015. **7**(1): p. 600-626.
4. Anderson, N., et al. *Design of an ultra-portable field transfer radiometer supporting automated vicarious calibration*. 2015. Proc: SPIE Vol. 9607 p. 960709-960709-9
5. Thome, K.J., et al. *Preflight and Vicarious Calibration of ARTEMIS*. in *Geoscience and Remote Sensing Symposium, 2008. IGARSS 2008. IEEE International*. 2008. Proc: IEEE Geoscience and Remote Sensing Symposium (IGARSS) Vol. 1 p. I-249 - I-252
6. Czapla-Myers, J., et al., *Earth-observing satellite intercomparison using the Radiometric Calibration Test Site at Railroad Valley*. Journal of Applied Remote Sensing, 2017. **12**(1).
7. Berk, A., et al. *MODTRAN6: a major upgrade of the MODTRAN radiative transfer code*. in *SPIE*. 2014. Proc Vol. 9088 p. 90880H-90880H-7
8. Biggar, S.F., et al. *Laboratory calibration of field reflectance panels*. 1988. Proc: SPIE Vol. 924 p. 232-240
9. Ehsani, A.R., J.A. Reagan, and W.H. Erxleben, *Design and Performance Analysis of an Automated 10-Channel Solar Radiometer Instrument*. Journal of Atmospheric and Oceanic Technology, 1998. **15**(3): p. 697-707.
10. Czapla-Myers, J., K. Thome, and S. Biggar. *Unmanned vicarious calibration for large-footprint sensors*. in *Earth Observing Systems X*. 2005. San Diego, CA, USAProc: SPIE Vol. 5882 p. 588218-10
11. Holben, B.N., et al., *AERONET - A Federated Instrument Network and Data Archive for Aerosol Characterization*. Remote Sensing Environment, 1998. **66**: p. 1-16.
12. Abdelatif, A., et al. *Prism spectrometer analysis for field use*. in *SPIE Optical Engineering + Applications*. 2018. Proc: SPIE Vol. 10764 p. 10

13. Abdelatif, A., *Off-Grid Field Deployable Prism Spectrometer*, in *James C. Wyant College of Optical Sciences*. 2019, University of Arizona.
14. Hankerson, J., *Automated Motion Control of a Ground-Viewing Radiometer System*, in *Wyant College of Optical Sciences*. 2018, The University of Arizona: Tucson, AZ, USA.
15. Czapla-Myers, J. and E. Woolliams, *Uncertainty Analysis Statement – RVUS*. 2018.
16. Thome, K., et al. *Calibration and use of an ultra-portable field transfer radiometer for automated vicarious calibration*. in *SPIE Optical Engineering + Applications*. 2017. Proc: SPIE Vol. 10402 p. 11